Dynamic behaviour during liquid-liquid phase separation within 2D confinement

by

Gilmar Friedrich Arends

A thesis submitted in partial fulfillment of the requirements for the degree of

Master of Science

in

Chemical Engineering

Department of Chemical and Materials Engineering
University of Alberta

Abstract

Fluid transport within confinement is important for many lab-scale and industrial-scale technological processes ranging from membrane separation, enhanced oil recovery, CO_2 sequestration to drug delivery systems. At the industrial scale, confined liquids are often quite complex as they consist of several chemical components and phases. The physicochemical properties of the confined fluid and displacing fluid can impact fluid transport in many ways. More specifically, differences in the solubility of species can drive liquid-liquid phase separation, which often results in chemical composition gradients influencing the displacement rate. One of the major challenges is to improve fluid transport in confinement which is primarily driven through diffusion.

The work in this thesis explores the effects of liquid-liquid phase separation on the displacement process of confined ternary liquid mixtures in a quasi-2D microchannel. The ternary mixtures consisted of a model oil component, a good solvent (ethanol) and a poor solvent (water). The mixtures were displaced and diluted by a penetrating liquid consisting of water or ethanol aqueous solution. The first part of the work reveals that the initial ternary solution composition affects the spatial distribution of subphases formed by phase separation and the displacement rates of the solutions producing distinct phase separation behaviours. The boundary between the confined ternary liquid and the penetrating liquid changes from a defined interface to a diffusive interface by reducing the initial 1-octanol composition. The boundary displacement rate was found to vary non-linearly as a function of the initial 1-octanol solution composition. The slowest boundary displacement rates were found at an intermediate 1-octanol composition. However, the rate was still 2 times faster than

expected for a purely diffusive process. At low 1-octanol compositions (2-20 wt-%), fast displacement rates were associated with droplet formation and movement driven by local composition gradients formed during phase separation.

The second part of the work investigates the direction and speed of propelling microdroplets driven by local chemical composition gradients from liquid-liquid phase separation within confinement. The microdroplets, $\sim 1/4 - 1/3$ the height of a narrow channel, form and move spontaneously as the ternary solution mixes with water diffusing from a deep side channel. The local composition gradients were estimated from fluorescence intensity measurements, and microdroplet movement was followed in situ using high-speed bright field imaging. From the phase separation of a ternary solution with high oil composition, propelling oil-rich microdroplets formed within a water-rich phase zone, along with water-rich microdroplets in an oil-rich phase zone. The oil-rich propelling microdroplets induce a directional flow transport that mobilizes water-rich microdroplets close to water-rich zones. Microdroplet displacement scaled linearly with time regardless of the solution compositions, while average droplet speed increased with initial oil composition displaying speeds up to 150 $\mu m/s$ along the surface of the hydrophobic wall. The presence of a sharp ethanol concentration gradient is believed to be the primary driving force for the fast movement of oil-rich microdroplets. Overall, the knowledge gained from this thesis improves the understanding of fluid transport within confinement, particularly for systems undergoing liquid-liquid phase separation. The work highlights the potential of using phase separation as a functional strategy to improve multicomponent liquid flow within confinement applicable for a wide range of separation processes.

Preface

This thesis is an original work by me, Gilmar F. Arends. The chapters in this work contain modified sections of the three following works:

1. Published work J. Qian, **G. F. Arends**, and X. Zhang. Surface nanodroplets formation, dissolution, and applications, Langmuir 35 (2019) 12583-12596. I was the second author for this invited feature article and was responsible for writing 3 major sections of the work and assisting in the overall manuscript edits. Modified sections of this work were used as background information in Chapter 1.

   The work is available at https://doi.org/10.1021/acs.langmuir.9b01051

2. Published work **G. F. Arends**, J. B. You, J. M. Shaw, X. Zhang. Enhanced displacement of phase separating liquid mixtures in 2D confined spaces, Energy & Fuels. 35 (2021) 5194–5205. I was the main author of the work and was responsible for all the data collection and analysis and writing up the manuscript. J. B. You assisted in the manuscript edits. J. M. Shaw and X. Zhang were both supervisory authors and were involved with the manuscript structure and edits. Modified sections of this published journal article were used for Chapter 1 as background information, Chapter 2 for the experimental methods and Chapter 3 for results, discussion and conclusion. In addition, relevant supplemental information was added as Appendices A to C.

   The work is available at https://doi.org/10.1021/acs.energyfuels.1c00139

3. Work submitted under **G. F. Arends**, J. M. Shaw, X. Zhang. How fast do

microdroplets generated during liquid-liquid phase separation move in a confined 2D space?, Energy & Fuels. (2021). I am the main author of this work and was responsible for collecting and analyzing the data and writing up the manuscript. J. M. Shaw and X. Zhang were both supervisory authors contributing intellectually and were involved with the manuscript composition. Modified sections of this work were used in Chapter 1 and Chapter 2. The Results and Discussion, and the Conclusions sections of this work were added as Chapter 4 to this thesis.

This work is dedicated to my opa, Feliciano Arends.

Acknowledgements

First and foremost, I would like to express my sincere gratitude to my supervisors, Drs. Xuehua Zhang, and John M. Shaw. Thank you for your patience, support and wisdom shared with me throughout my graduate studies. Dr. Zhang provided me with the amazing opportunity to be part of her group, which I will never forget. I learned a great deal under her supervision, and she always pushed me to be the best I could be. Dr. Shaw always provided me with insightful feedback that pushed me to sharpen my thinking and brought my work to a higher level.

I am also grateful to have worked with Drs. Jiasheng Qian and Jae B. You. Without their guidance, advice and support, this thesis work would not have been possible.

I would like to thank all the present and previous members of the Soft Matter and Interfaces group I had the opportunity to work with. I appreciate all the advice and support they provided me.

I would also like to acknowledge the financial support obtained from the Natural Science and Engineering Research Council of Canada (NSERC) and Future Energy Systems (Canada First Research Excellence Fund).

To my parents, Anabel and Guido, and grandparents, Feliciano and Maria Jeanette Arends. Thank you for always encouraging me to pursue my dreams. Without your love and constant support, this work would not have been possible.

Finally, to my girlfriend, Laura Gabler. Thank you for your patience, love and for always believing in me. I look forward to our next adventure together, especially with our little Skye by our side.

Table of Contents

List of Tables

List of Figures

List of Symbols

D Effective diffusion constant

F_D Compound drag force by the surface effects

F_M Shear force related to the Marangoni flow

F_{vis} Viscous force by surrounding liquid

$I(d)$ Mean gray intensity as function of position d along triangular protrusion

$I(x)$ Mean gray intensity as function of position x

I_0 Mean gray intensity at side channel position $x = 0$

I_{df} Mean gray intensity at final position df, at the water-rich side of a triangular zone

I_{di} Mean gray intensity at position $d = 0$, starting along fixed y-position at the center of a triangular zone

$I_{norm}(d)$ Normalized intensity across triangular protrusion as function of position d

Ma Marangoni number

P Pressure

Q_b Solution B flow rate

Q_k Dortmund UNIFAC Van der Waals group surface area

R Droplet radius

R Gas constant

R_k Dortmund UNIFAC Van der Waals group volume

T Temperature

X_m Group mole fraction of group m in liquid phase

$\Delta\rho_{eth}$ Ethanol mass concentration change in surrounding liquid

$\Delta\sigma$ Difference in surface tension

Γ_k Group activity coefficient of group k in the mixture

Ψ_{nm} UNIFAC group interaction parameters between groups n and m

γ Surface tension

μ Viscosity of liquid surrounding the droplet surface

ω Triangular protrusion angle

ρ Surrounding liquid density

θ Droplet propulsion angle

θ_m Surface fraction of group m in liquid phase

$a(x)$ Fitting parameter for normalized intensity profile at fixed x-position and time

a_{nm}, b_{nm}, c_{nm} Dortmund UNIFAC interaction parameters based on groups m and n

d Position along data acquisition line perpendicular to triangular protrusion

d_{final} Final position of water-rich droplets where they merge at boundary between zone 2 and 3

h^E Molar excess enthalpy

l Displacement (boundary or droplet)

n Exponent value from linear regression fit

t Time

$w_{eth12,1}$ Ethanol mass fraction at the boundary 1 between zone 1 and 2

$w_{eth12,2}$ Ethanol mass fraction at boundary between 1 and 2 at zone 2 side

$w_{eth12,2}$ Ethanol mass fraction at the boundary 2 between zone 1 and 2

$w_{eth23,2}$ Ethanol mass fraction at boundary between 2 and 3 at zone 2 side

$w_{eth23,2}$ Ethanol mass fraction at the boundary 2 between zone 2 and 3

$w_{eth23,3}$ Ethanol mass fraction at boundary between 2 and 3 at zone 3 side

$w_{eth23,3}$ Ethanol mass fraction at the boundary 3 between zone 2 and 3

w_{eth} Ethanol mass fraction

x Position along x-direction

x_0 Initial position at triangular protrusion tip

x_i Mole fraction of component i in the liquid phase

$\Gamma_k{}^{(i)}$ Group activity coefficient of group k in the pure substance

$\nu_m{}^{(i)}$ Number of structural groups of type m in molecule i

Abbreviations

BP Butyl paraben.

Exp. Experiment.

F.O.V. Field of view.

FPS Frames per second.

HDODA 1,6-Hexanediol diacrylate.

LLPS Liquid-liquid phase separation.

OTS-Si Octadecyltrichlorosilane treated silicon wafer.

UNIFAC UNIQUAC Functional-group Activity Coefficients.

Chapter 1

Introduction

1.1 Background

1.1.1 Fluid flow transport within confinement and its relevancy[1]

Efficient fluid transport within narrow spaces is relevant to many technological applications, including enhanced oil recovery [1–4], nuclear waste storage [5], geothermal energy production [6], carbon capture [7], CO_2 sequestration [8, 9], catalytic-based chemical conversion [10], porous membrane separation [11], water treatment [1, 12, 13], and drug delivery systems [14–18]. In confined spaces, liquid mixing is dominated by slow mutual diffusion [19, 20] influenced by the physical properties of liquids. Extensive studies have been performed to understand the effects of wettability of the wall surface [13, 20, 21], fluid viscosity [2, 22], or interfacial tension of immiscible phases [9, 23].

In conventional crude oil recovery processes, the displacement of oil occurs through pressure-assisted methods (primary method) or through water and gas injections into reservoirs (secondary method) [24]. Both traditional methods are only able to recover up to 40% of oil from reservoirs [24, 25]. Typically, the remaining oil is microscopically trapped in porous rocks. The extraction of oil in such situations is controlled by

[1] This section contains modified parts of published work by **G. F. Arends**, J. B. You, J. M. Shaw, X. Zhang. Enhanced displacement of phase separating liquid mixtures in 2D confined spaces, Energy & Fuels. 35 (2021) 5194–5205.

phenomena occurring at the microscopic-level scale where the geometry of the pore structures and the physicochemical properties of the confined fluid have a great impact on the displacement process [24, 26, 27].

Confined liquids to be displaced are generally complex as they consist of multiple chemical components and phases that can all affect fluid transport behaviour [27, 28]. Chemical flooding methods for enhanced oil recovery use carefully selected displacing fluids that manipulate the properties of the confined fluid to recover the entrapped oil phase from porous rocks. The displacing fluid may include plugging agents that can direct oil towards desired locations, acids that etch the pore walls, chemicals that influence the viscosity and surfactants that alter the wettability and interfacial tension [25, 28, 29].

In surfactant flooding, emulsions and microemulsions form as intermediates by the displacement process [30]. Several studies have indicated improvements in recovery efficiency from porous media when microdroplet emulsions are formed during displacement compared to cases without emulsion formation. The enhancement effect was attributed to the desired rheological properties and seepage characteristics of surfactant-stabilized microdroplets [31]. Additionally, microdroplets show promising dynamic behaviours, particularly within chemical systems far out of equilibrium, which can ultimately be leveraged to improve fluid transport within confinement. It is important for both fundamental understanding and practical applications to obtain new methods to achieve fast fluid movement in confined spaces [23].

1.1.2 Microdroplet formation through liquid-liquid phase separation

Overview of emulsification processes

Emulsions have various applications in the pharmaceuticals [32], food industry [33] and geoscience fields [30]. Macroemulsions are commonly prepared in bulk through active mixing of two immiscible phases (i.e. water and hydrophobic substances) and

are stabilized with surfactants [34]. When immiscible phases are initially in thermodynamic equilibrium, external mechanical or thermal energy must be applied to exceed the kinetic barrier needed to form emulsions Figure 1.1A [35]. The formation barrier is related to the reversible work, or Gibbs free energy (dG) needed to expand the interface between the phases, which is given as a product of the interfacial tension (γ in N/m) and change in the interfacial area (dA in m^2) [35, 36].

Emulsification can also occur spontaneously without requiring any source of external energy ($\Delta G < 0$) Figure 1.1B [35]. For example, in-situ spontaneous formation of microemulsions occurs as bulk liquids are not in equilibrium caused by stagnant flow within confinement. In these cases, gradients in chemical potential between the phases are enough to drive the spontaneous emulsification when immiscible or partially miscible phases are brought into contact [34]. The dynamic transport process that is driven by the chemical potential gradient is better known as diffusion. The mixing dynamics and the thermodynamic properties are equally important for the spontaneous emulsification process, as will be discussed in the following sections.

A stabilization kinetic barrier determines the energy at which emulsions finally phase separate into two bulk phases Figure 1.1 [35]. Macroemulsions have a low stabilization kinetic barrier as they are thermodynamically unstable, resulting in complete phase separation in order to decrease the interfacial energy between the phases [37]. By contrast, microdroplets formed from spontaneous emulsification are thermodynamically metastable. These microdroplets remain stable for a longer time due to the larger kinetic barrier to phase separation [38].

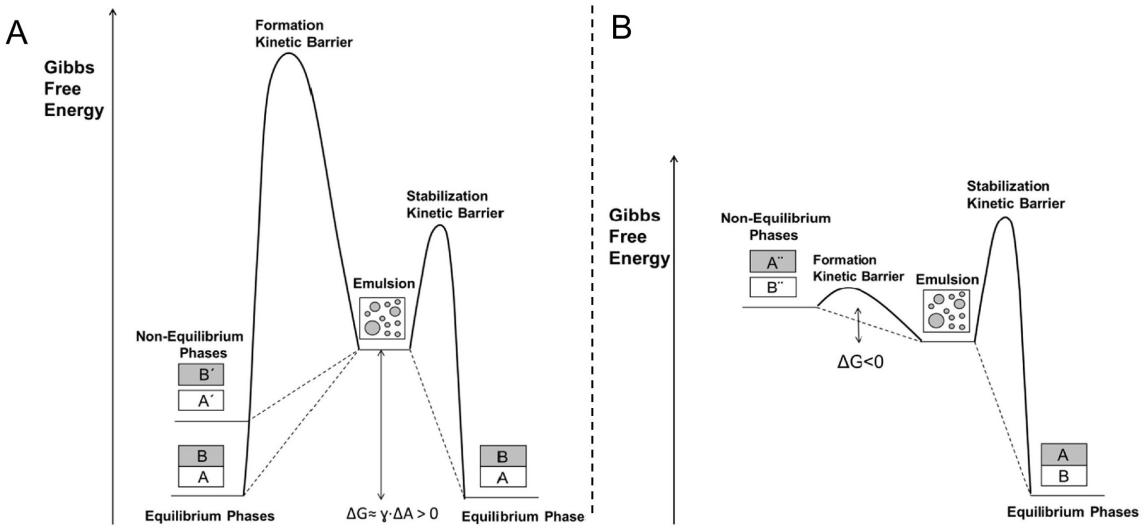

Figure 1.1: Illustration of Gibbs free energy profile for emulsion formation by (A) applying external energy or (B) spontaneously through internal energy [35].

Thermodynamics of liquid-liquid phase separation of a ternary system

In ternary liquid mixtures, deviations in temperature, concentration, pH, ionic strength, or pressure can drive liquid-liquid phase separation (LLPS), where a condensed and dilute phase are formed [39, 40]. The thermodynamic driving force for phase separation is the minimization of Gibbs free energy of an unstable mixture. Figure 1.2A shows a typical ternary phase diagram consisting of a mixture of oil, water, and a hydrotrope (miscible with both components) [41]. The outer solid curve indicates the binodal curve or miscibility-limit curve, which describes where single-phase mixtures transition to a metastable or unstable two-phase liquid. The dashed line indicates the spinodal curve, which separates the unstable regions from the metastable regions within the two-phase zone. The intersection of the binodal and spinodal curves is called the Plait point and indicates the point where two phases with the same composition will coexist [35, 41].

Depending on the initial liquid composition, different phase behaviour can be expected. Above the binodal curve, all ternary compositions result in single-phase mixtures. Within the two-phase zone, tie-lines indicate the equilibrium compositions

of the dilute phase (c_D) and the condensed phase (c_C) after phase separation (Figure 1.2B). Along the same tie-line, every mixture will separate into two phases with fixed compositions but in different quantities. If the initial composition lies between the binodal and spinodal curves, the liquid will separate through droplet nucleation (Figure 1.2C). For the two compositions indicated in the water-rich metastable region (Figure 1.2B), droplet size is controlled by the relative volume of the dilute phase compared to the condensed phase, which can be approximated using the lever rule (Figure 1.2D). Compositions within the water-rich metastable region (green) produce oil-rich droplets, while those in the oil-rich region (yellow) produce water-rich droplets. The composition at the center of the two-phase region (blue) indicates phase separation through spinodal decomposition, where no droplet nucleation occurs and phase change occurs immediately [40].

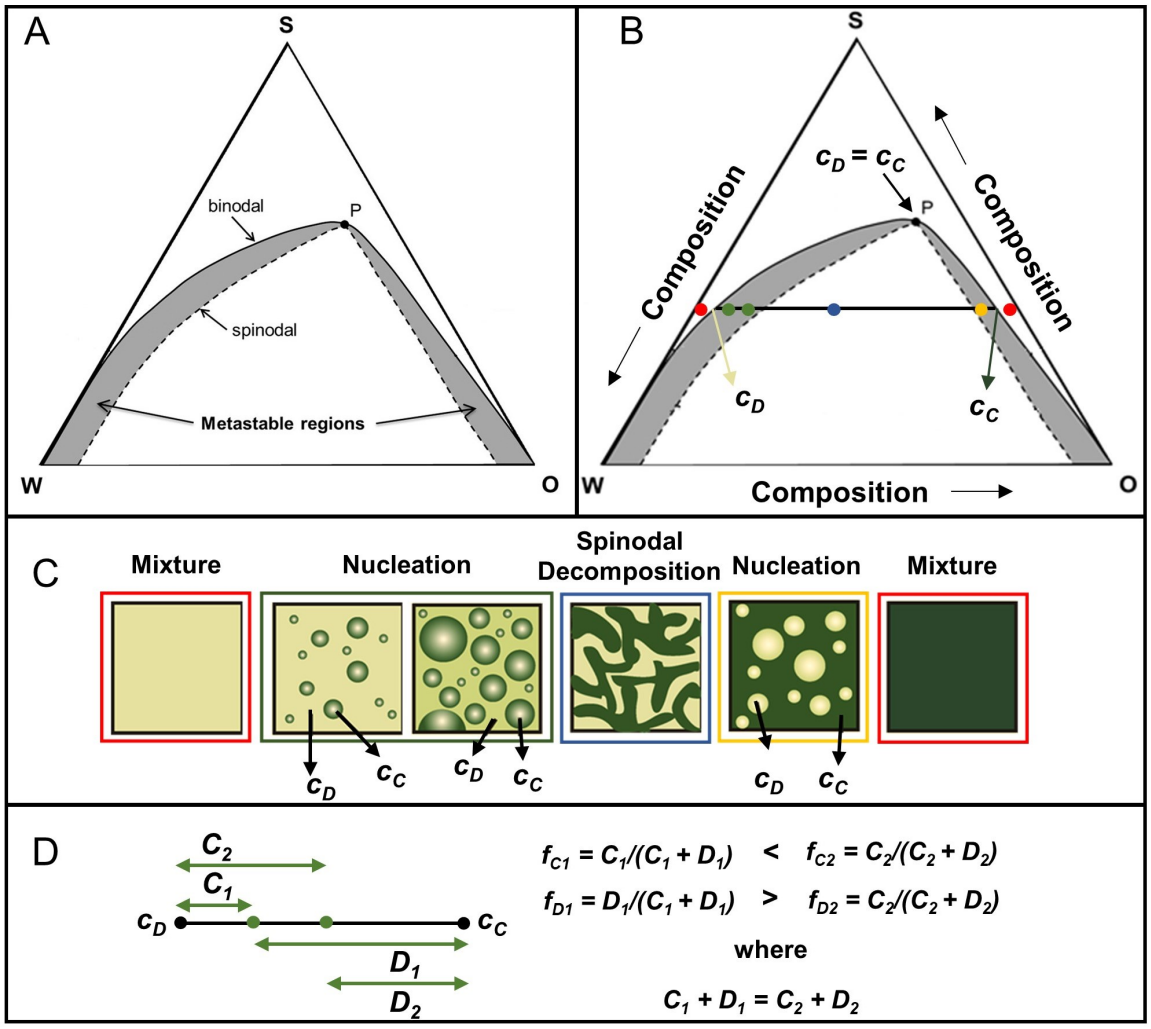

Figure 1.2: Ternary phase diagram indicating the (A) binodal, spinodal and metastable regions for an oil, water and hydrotrope chemical system. (B) A representative tie line indicating several initial compositions used to show the different phase behaviour in (C). (D) The lever rule indicates the relative volume of two compositions on the same tie line. c_D represents the dilute phase composition (water-rich), and c_C is the condensed phase composition (oil-rich). f_c and f_d represent the volume fractions of the condensed phase and dilute phase. Modified from [35, 40].

Droplet formation through the Ouzo effect

When water is added to a mixture of anise oil and ethanol, small droplets spontaneously nucleate, making the entire solution appear milky. This physical phenomenon was termed the "Ouzo effect" by Vitale et al. after the Greek alcoholic beverage

named Ouzo [38]. The formation of droplets occurs when the composition of the single-phase solution is rapidly shifted to the metastable region between the spinodal and binodal curves by adding a poor solvent – changing the solubility of some components more than others. The Ouzo effect occurs through homogeneous droplet nucleation resulting in a uniform dispersion of stable droplets within the entire continuous phase [38, 41].

More specifically, the formation and dispersion of droplets are driven by the supersaturation (also known as diffusion-stranding mechanism) of the solute by minor local fluctuations in concentration [35, 38]. These fluctuations result in nuclei formation with a large average concentration of the solute, exhausting the solute from the surroundings. Subsequent nucleation of droplets occurs only at locations where the supersaturation level is large enough, typically far from other nuclei. The process of nucleation ceases after no more regions of supersaturation exist. Once the droplets are formed, they grow through Ostwald ripening, where small droplets dissolve, and nearby larger ones grow by diffusion of the dissolved droplet liquid [38].

The solvent exchange method[2]

Simple surfactant-free systems are often used to study and control the nucleation and growth of nano- and micro-sized droplets [35]. Typically, the solvent exchange method is used as a convenient bottom-up approach to produce surface nanodroplets from the displacement and mixing between two solutions within a microfluidic device [42]. This method is very robust as it can be used to produce droplets with a wide selection of oils and solvents (Table 1.1). The oil component can be small hydrophobic organic molecules, alcohols, lipids or polymers dissolved in polar organic solvents [43]. The main requirement for the solvent exchange method is to find a solvent combination where one solvent is immiscible with the droplet liquid and the second is a co-solvent.

[2] This section contains modified parts of published work by J. Qian, **G. F. Arends**, and X. Zhang. Surface nanodroplets formation, dissolution, and applications, Langmuir 35 (2019) 12583-12596.

Table 1.1: List of model compounds used in the solvent exchange method [42–48].

Droplet Phase	**Examples**	**Solution A**	**Solution B**
Alcohols	3-heptanol, 1-octanol	ethanol aqueous solution	water
Alkanes	hexadecane, decane, cyclohexane	ethanol aqueous solution	water
Fatty acids	oleic acid, lauryl acid, palmatic acid	ethanol aqueous solution	water
Other oil phases	vitamin E, toluene, anise oil	ethanol aqueous solution	water
Acrylate monomers	lauryl methylacrylate, 1,6-hexanediol di-acrylate,	ethanol aqueous solution	water
Polymers	poly(dimethylsiloxane) PDMS	tetrahydrofuran THF	water
Water		ethanol in octanol or cyclohexane	octanol or cyclohexane

In the solvent exchange method, surface droplets are nucleated on a substrate (with suitable wettability for the droplet liquid) by adding a poor solvent (solution B) into a solution consisting of a large ratio of good solvent to oil (solution A). When solution A is displaced by solution B, the mixture becomes oversaturated by oil at the mixing front (Figure 1.3). At this location, the ternary composition changes from the single-phase region to the metastable Ouzo region with a constant oil to good solvent ratio [42, 49]. The change in composition results in many droplets forming over a large surface area on the solid substrate by the Ouzo effect [38, 41, 43]. The overall saturation level oil is determined by the area between the dilution curve and the binodal curve (Figure 1.4A). At high oil to solvent ratios, the dilution process may result in direct local phase separation as the dilution curve crosses the spinodal region. The oil-rich subphase that is formed is immiscible with the displacing fluid

and is simply washed away. The water-subphase can further mix with the displacing fluid, subsequently forming Ouzo droplets (Figure 1.4B) [42, 46].

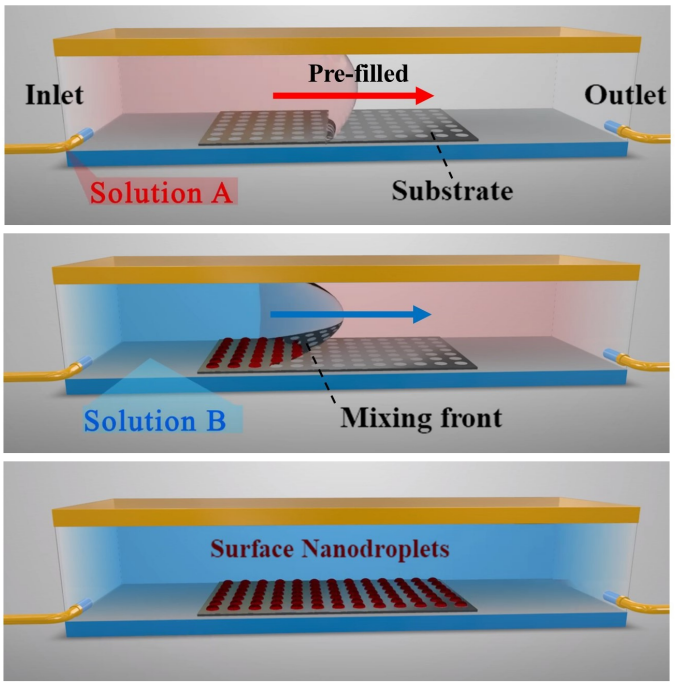

Figure 1.3: Illustration of the solvent exchange process. Created and modified from [50].

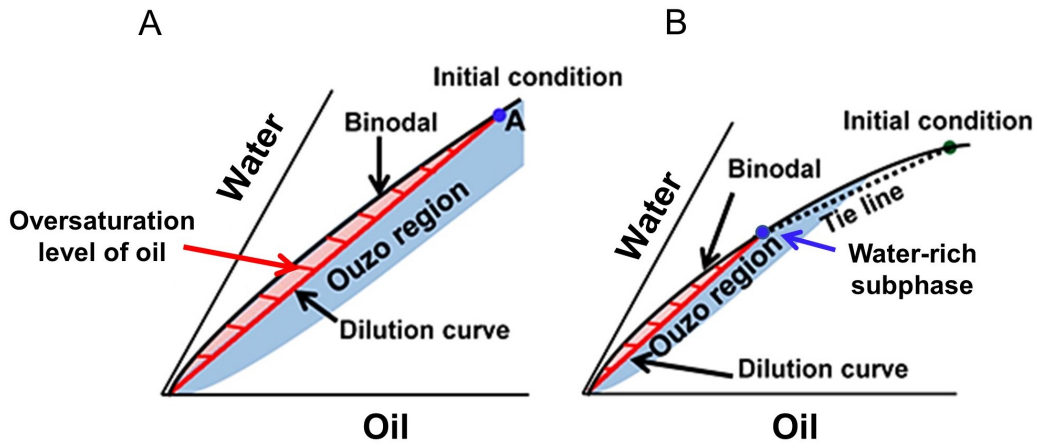

Figure 1.4: Sketch of a dilution curve indicating oversaturation level during the solvent exchange. (A) The red region indicates the oversaturation level of oil between the binodal and dilution curve. (B) If the initial solution is outside the Ouzo region, droplets will form from the consequent dilution of the water-rich phase. Modified from [45, 46].

One advantage of the solvent exchange method is that the exact composition of the droplet liquid can be manipulated according to the ternary phase diagram. Furthermore, the morphology of the droplets can be fine-tuned with several macroscopic level parameters [42], as summarized in Table 1.2. By significantly reducing the channel height to only a few microns, the transport and mixing between solutions A and B will occur primarily through diffusion. The effects of external mixing of the bulk fluid are thus eliminated, making it possible to imitate the conditions of fluid flow within confinement [43]. This method provides a way to unravel the effects of droplet nucleation by liquid-liquid phase separation and local chemical composition gradients within confinement [51].

Table 1.2: List of typical parameters used to control the characteristics of the droplets in the solvent exchange method. [42, 45, 46, 48, 49, 52–57]

Main Parameters	**Influences**	**Controls**
Initial solution composition	Oversaturation level of droplet liquid	Droplet composition and volume
Flow rate	Mass transport between A and B	Droplet volume
Channel height	Gravitational effects	Droplet growth time, volume distribution
Surface wettability	Contact angle, nucleation sites	Surface coverage and droplet morphology
Temperature	Viscosity, phase behaviour	Size, number density, phase behaviour for droplet formation

1.1.3 Enhanced fluid transport by microdroplets[3]

The creation and movement of microdroplets in confinement hold promise for improved fluid transport in enhanced oil recovery processes[1, 31, 58], novel chemical analysis techniques [59], drug and gene delivery systems [60], smart colloid transportation [61–66], and chemical synthesis [67, 68]. Recently, the autonomous motion of microdroplets has attracted research interest, due to the potential to imitate numerous forms of life-like and robotic behaviours [61, 69, 70]. For example, droplets may display individual [71, 72] or collective chemotactic behaviour [73, 74], controlled clustering [75] and the capability of carrying payloads through complex geometries [69, 72, 76]

The common mechanisms for the autonomous motion of droplets involve a Marangoni effect induced by surface tension gradients [64, 70, 77–82]. Droplets can travel over a long distance as long as the driving force from the unequilibrated chemical constituent can be sustained. Microdroplet motion can potentially reach high speeds and in designated directions by manipulating surface tension gradients around them. These gradients may be generated by many chemical approaches, including changes in the local pH [63, 83], surfactant concentration [72], the concentration of chemically reactive species or products [84], or combinations of the above.

For example, in the work by Thutupalli et al. [74], a reactant-containing water droplet is in contact with an oil phase containing a surfactant. The reactant in the droplet reacts with the surfactant at the droplet surface, leading to increased local surface tension. A Marangoni flow along the droplet surface propels the droplet and replenishes the reacting droplet surface with fresh surfactant. The self-sustaining droplet motion continues until the reactant in the droplet is exhausted.

A dimensionless Marangoni number (Ma) is often used to provide a quantitative

[3] This section contains modified parts of work submitted as **G. F. Arends**, J. M. Shaw, X. Zhang. How fast a self-propelling microdroplet moves during liquid-liquid phase separation confined in 2D space?

comparison between the rate of transport by Marangoni flow versus the rate of transport by diffusion [51]. A large Ma means transport is dominated by a surface tension gradient, resulting in large Marangoni flow velocities. The speed of microdroplets reported in the literature ranges from 10 to 10^4 $\mu m/s$ [76, 83, 85], depending on the droplet size and driving force of the autonomous motion.

Concentration gradients for the autonomous motion of droplets can also arise through spontaneous phase separation in multicomponent mixtures. The concentration gradient in a ternary ouzo solution can be sufficient to drive a macroscopic drop to oscillate or jump against gravity [78, 86]. Li et al. reported the fascinating jump and sudden death of a sub-millimetre oil drop in vertically stratified ethanol + water mixture [78]. The sharp ethanol concentration gradient induces a Marangoni flow that propels the droplet to repeatedly jump up to about 10 times of droplet size, which then falls under gravity. The cycle of jumping and falling repeats at a frequency of 2–3 Hz and lasts for approximately 30 minutes until the concentration gradient decays [78]. Sudden death occurs when the Marangoni flow is not able to sustain the jumping behaviour and buoyancy dominates. What controls the speed of propelling droplets in confined spaces is an important and unresolved question.

1.2 Motivation

The development of new methods to understand and improve fluid transport within confined spaces for multicomponent and multiphase systems is relevant to many processes. Lu et al. [43], determined that the formation of microdroplets through the Ouzo effect can enhance the liquid transport within quasi-2D confinement. The effect was demonstrated for a small range of ternary solution compositions limited to the Ouzo region. It is still unclear how the composition and relative amounts of subphases formed by liquid-liquid phase separation can influence the liquid transport within confinement. This work investigates the effects of liquid composition on the displacement process of ternary liquid mixtures undergoing liquid-liquid phase sepa-

ration with a penetrating liquid phase within 2D confinement. The experiments show distinct phase separation behaviour occurs influenced by the composition changes. Several dynamic events at macroscopic and microscopic levels are observed in situ through optical and fluorescence microscopy. Macroscopic processes were mainly influenced by the boundary behaviour between the penetrating liquid and the confined liquid, while microscopic processes were influenced by local composition gradients driven by the slow mixing dynamics. The work highlights the importance of controlling phase separation to improve liquid transport within confinement.

1.3 Thesis objectives

The overall goal of this thesis is to investigate the displacement process of a model ternary liquid mixture within a 2D microfluidic chamber where phase separation occurs concurrently by mixing with a penetrating liquid. The individual objectives of this thesis work are as following:

1. To modify the solution compositions of the confined and penetrating phases to evaluate the effect of the newly formed subphases from liquid-liquid phase separation on the displacement process.

2. To determine the ternary liquid compositions that result in the fastest displacement rates as observed from the boundary movement between the solutions and to examine how the energy from phase separation is related to the displacement rate.

3. To compare the displacement process of a confined single-component liquid displaced by a ternary solution.

4. To examine the effects of solution composition on the microscopic level dynamic events of droplet motion.

5. To approximate the composition gradients with fluorescence microscopy measurements.

6. To explore how the shape of the phase separation zone or mixing front is related to the direction and speeds of droplets formed by liquid-liquid phase separation during the displacement process.

1.4 Thesis outline

Chapter 1 provides a brief introduction on the relevancy of fluid flow within confinement, the formation of microdroplets through liquid-liquid phase separation and capabilities of improving liquid transport within confinement through microdroplet motion. The motivation and objectives of the thesis are also introduced in this chapter. Chapter 2 provides the experimental procedures, equipment and calculation methods used to obtain the results given in Chapters 3 and 4. Chapter 3 presents the experimental results and discussions for the study on the enhanced displacement of phase separating ternary liquid mixtures within confinement. Chapter 4 elaborates on the microscopic level events of droplet motion that occur with the displacement of phase separating ternary mixtures within confinement. Chapter 5 summarizes the two works discussed in Chapters 3 and 4 and finalizes with potential future works that could help determine other important parameters that affect phase separating multicomponent systems in confinement.

Chapter 2

Methods and procedure[1]

2.1 Chemicals and solution preparation

Solution A, the solution present in the 2D microchannel, comprised a mixture of 1-octanol (ACS grade >95%, Fischer Scientific), ethanol (Histological grade, Fischer Scientific) and water (Milli-Q). Solution B, the penetrating liquid, was water, a poor solvent for octanol. The detailed compositions of solution A containing octanol as the model oil, are listed in Table 2.1 and are labelled in the ternary phase diagram Figure 2.1A. Additional experiments were performed with variations to both confined and displacing liquids as listed in Table 2.2. Butylparaben (>99%, Sigma-Aldrich), 1,6-hexanediol diacrylate HDODA (>98.5% total reactive esters, Fisher Scientific - Alfa Aesar) and oleic acid (>99.0%, Fisher Scientific - Alfa Aesar) were used as alternative model oils in solution A.

A lipophilic stain Nile Red (Fischer Scientific) was added to solution A, at $1.0 \times 10^{-5} M$, so that the oil-rich phase could be identified from the fluorescence intensity of the dye after liquid-liquid phase separation. This dye partitions 99.9% to the octanol-rich subphase phase once it forms [87].

[1] This chapter is a combined and modified version of experimental sections in two works: 1) Published work, **G. F. Arends**, J. B. You, J. M. Shaw, X. Zhang. Enhanced displacement of phase separating liquid mixtures in 2D confined spaces, Energy & Fuels. 35 (2021) 5194–5205. 2) Submitted work, **G. F. Arends**, J. M. Shaw, and X. Zhang. How fast do microdroplets generated during liquid-liquid phase separation move in a confined 2D space? Energy & Fuels. (2021).

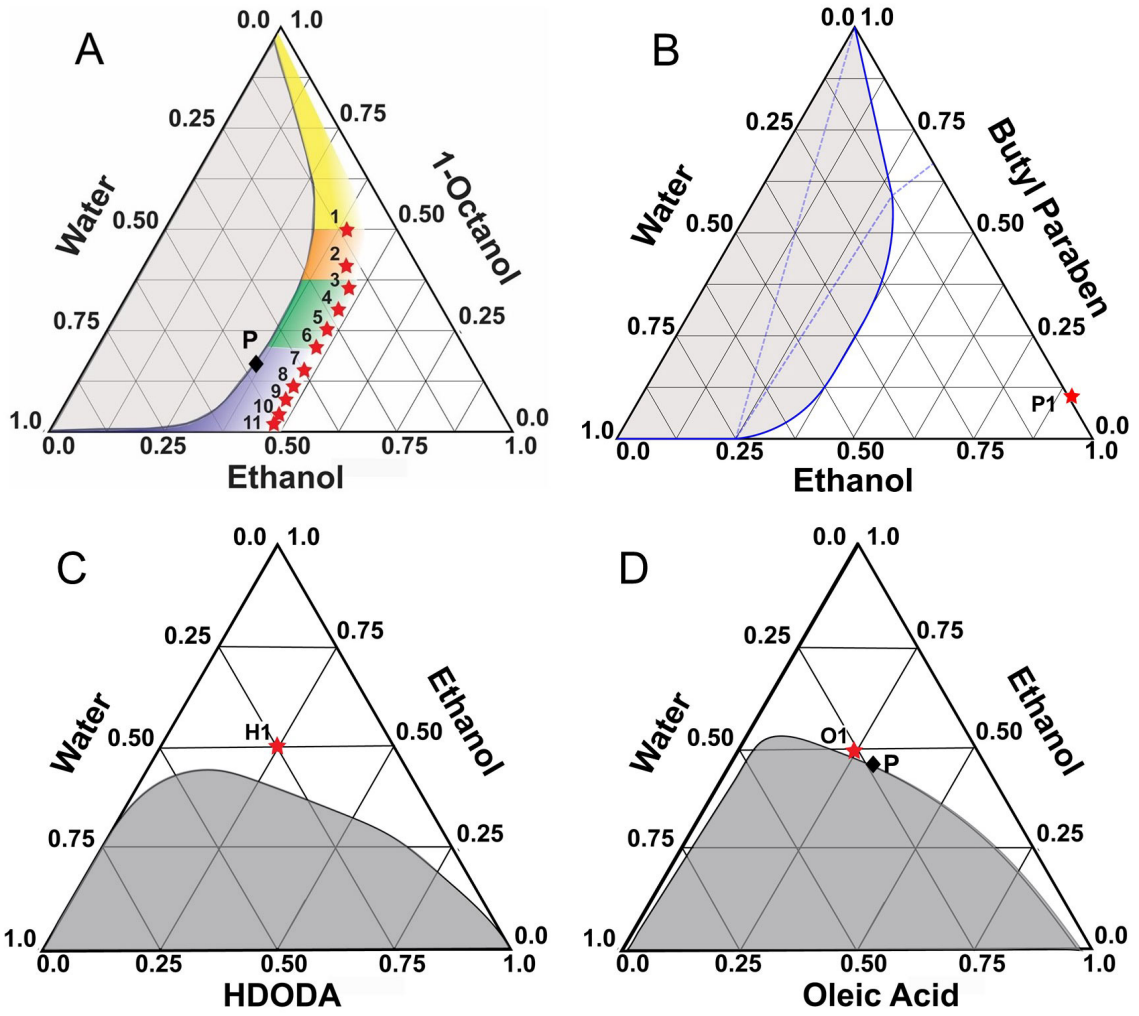

Figure 2.1: (A) Ternary phase diagram with composition regimes for the 1-octanol, ethanol and water ternary in terms of the mass fraction. The initial solution compositions are indicated with a star and annotated with the experiment number. The phase diagram was adapted from ref. [23]. Composition regimes are indicated as: Regime 1 (yellow), Regime 2 (orange), Regime 3 (green), and Regime 4 (blue). P indicates the Plait point ($L_1 = L_2$). (B) Ternary phase diagram for the butylparaben, ethanol and water ternary in terms of the mass fraction. Additional phase diagrams are for: (B) butylparaben, ethanol, water in mass fractions [88]; (C) HDODA, ethanol and water in mass fractions [89]; (D) Oleic acid, ethanol and water in mass fractions [90]. The initial solution compositions are indicated with a star.

Table 2.1: Experimental compositions of solution A (displaced liquid) with 1-octanol as the model oil.

Experiment	**1-Octanol** Mass %	**Ethanol** Mass %	**Water** Mass %
1	50	40	10
2	40	45	15
3	35	48	17
4	30	48	22
5	25	48	27
6	20	48	32
7	15	48	37
8	10	48	42
9	8	47	45
10	5	48	47
11	2	48	50

Table 2.2: Compositions of solution A (displaced liquid) and solution B (confined liquid) in additional experiments. Values are given in mass percentages.

	Solution A			**Solution B**		
Exp.	**1-Octanol**	**Ethanol**	**Water**	**1-Octanol**	**Ethanol**	**Water**
E1	50	40	10	0	25	75
E4	10	48	42	0	25	75
R1	0	0	100	50	40	10
R4	0	0	100	10	48	42
	BP	**Ethanol**	**Water**	**BP**	**Ethanol**	**Water**
P1	10	90	0	0	0	100
	HDODA	**Ethanol**	**Water**	**HDODA**	**Ethanol**	**Water**
H1	25	50	25	0	0	100
	Oleic Acid	**Ethanol**	**Water**	**Oleic Acid**	**Ethanol**	**Water**
O1	24	49	27	0	0	100

2.2 Experimental setup and wall surface properties of the quasi-2D microchamber

A microchannel was used to provide a quasi-2D space for the diffusive mixing between solutions A and B, as shown in Figure 2.2A. The flow chamber consisted of a polycarbonate base (8.5 cm $\times$ 4.5 cm $\times$ 1 cm), with a hydrophilic cover glass as the top sealed with a silicon rubber spacer. A hydrophobic silicon wafer was placed on the bottom base as the substrate. The exact dimensions of each component used in the microchamber are illustrated in Figure 2.2B and C.

Before any experimentation, every component from the chamber was sonicated in both water and ethanol for 10 minutes each. The chamber was assembled by connecting the tubing to the polycarbonate base as the inlet and outlet streams. A droplet of solution A was placed on the OTS-Si substrate. The substrate was held by a capillary bridge to the cover glass. A small confined channel height of around 20 to 30 μm was kept. The cover glass was then held in position by a spacer and was clamped to the base of the chamber with large binder clips.

The surfaces used for the experiments were hydrophilic glass slides (Fisherbrand Microscope Slides) and hydrophobic silicon wafers. Before use, both substrates were initially washed with piranha solution consisting of 70%-volume H_2SO_4 (ACS Plus grade, Fischer Scientific) and 30%-volume H_2O_2 (30% ACS grade, Fischer Scientific) at 85°C for 20 minutes. After the initial cleaning procedure, the substrates were further cleaned and sonicated with water and ethanol each for 15 minutes. The silicon wafers were dried in the oven at 120°C for 2 hours before they were hydrophobized with octadecyltrichlorosilane (OTS-Si), as previously documented [91]. A 0.5%-volume of OTS in hexane mixture was used to soak the wafers for 12 hours at room temperature within a closed petri dish sealed with a bag. The OTS-Si substrates were then sonicated with hexane, acetone, and ethanol each for 10 minutes after the hydrophobization procedure to remove any excess OTS on the surface. Hydrophilic

glass covers were stored in water, while OTS-Si substrates were kept in a clean petri dish.

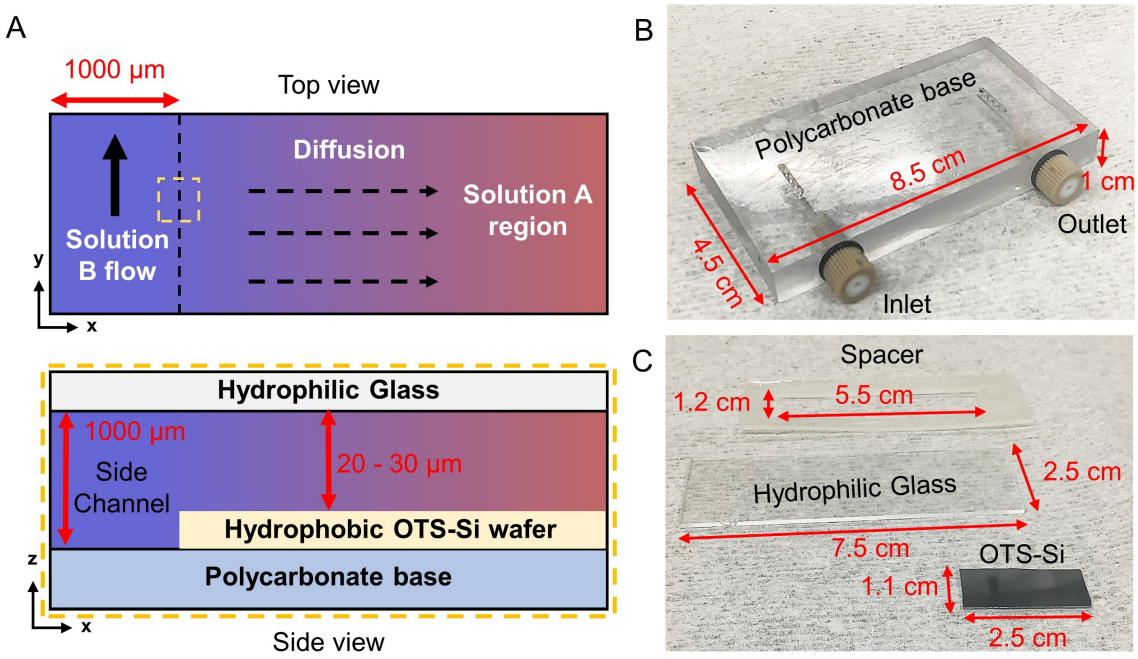

Figure 2.2: (A) Schematic of the fluid microchamber with top view and cross-section of the main and side channels. Dimensions of polycarbonate base (B), substrates and spacer (C).

2.3 Visualisation of liquid displacement and solvent mixing in the microchannel

The events occurring while solution B was pumped ($Q_B = 12\ mL/hr$) to the channel using a syringe pump (Fisherbrand Single Syringe Pump) were captured in situ with a camera (Nikon DS-Fi3) connected to an optical microscope (Nikon Eclipse Ni-U). Videos of the dynamic events were captured using an auto-exposure setting which resulted in framerates of 10 to 15 frames per second (FPS) with a fixed resolution of 2880 $\times$ 2048 pixels. Fluorescence videos were captured at a low framerate of 0.9 to 1 FPS due to longer exposure times needed. A high-speed camera (Photron Fastcam Mini UX100) was used instead to capture shorter time-scale or faster events. The high-speed camera captured videos at 500 or 1000 FPS for a duration of 4.5 seconds

at a resolution of 1280 × 1024 pixels.

2.4 Tracking and data analysis of dynamic events

The videos were processed through ImageJ (Fiji package) and were converted to image sequences in 8-bit grayscale. If required, the contrast and brightness levels were adjusted, and a bleach correction was applied. Liquid boundary and droplet tracking were performed manually with an ImageJ plugin. For high-speed image sequences, the tracking was performed at time intervals of 0.02 s. The spatial resolution was 0.24 μm/px for the Nikon DS-Fi3 camera and 1 μm/px for the Photron Fastcam Mini UX100 camera at a microscope magnification of 10×. The tracking data from ImageJ was saved as a CSV file, which included frame and position data in pixels. The displacement was calculated using the x and y positions using the first entry in the data set as the initial position.

At different solution compositions, there were distinct features to be analyzed. Oil-rich and water-rich droplets were tracked as they nucleated and became visible in the field of view. Tracking was terminated when droplets came to a stop or when they merged with nearby phase domains. Droplet displacement (l) was calculated from the x and y positions as a function of time (t) using the first entries in the data set ($t = 0$) as the initial positions where:

$$l(t) = \sqrt{(\Delta x^2 + \Delta y^2)} = \sqrt{[(x(t) - x(t=0)]^2 + [y(t) - y(t=0)]^2} \qquad (2.1)$$

2.5 Image analysis for local concentration gradient

The Marangoni number compares the transport related to the stress imposed by concentration gradients versus the transport related to diffusion. The dimensionless Marangoni number was used to relate droplet mobility to ethanol composition gradients within a given phase. The dimensionless Marangoni number Ma for a droplet

within 2D space is expressed as [51]:

$$Ma = \Delta\sigma \left(\frac{R}{\rho\nu D} \right) = \Delta\sigma \left(\frac{R}{\mu D} \right) \tag{2.2}$$

where R is the droplet radius or characteristic length in m, μ is the viscosity of the surrounding liquid in $Pa \cdot s$, and D is the diffusion constant in m^2/s. Due to the small length scale of the droplets, the viscosity is taken as a constant. The surface tension gradient is expressed as a function of x-position [51]:

$$\Delta\sigma \approx \frac{\partial\sigma}{\partial\rho_{eth}} \Delta\rho_{eth} \approx \frac{\partial\sigma}{\partial w_{eth}} \Delta w_{eth}(x) \tag{2.3}$$

where σ is the surface tension as a function of ethanol composition (w_{eth}). The surface tension values were approximated, based on local compositions, using the UNIFAC thermodynamic model within the software package Symmetry.

At a given time in the main channel, solution A, water, and subphases from phase separation evolve into two different configurations: a three-zone configuration (Figure 2.3A) and a triangular protrusion of solution A behind the receding boundary as sketched in Figure 2.3B. The local mass fraction of the good solvent (ethanol) was estimated from fluorescence intensity. The ethanol mass fraction (w_{eth}) is 0 at $x = 0$ defined as the closest point to the side channel where (dye-free) water is supplied. The increase in dye concentration close to $x = 0$ results in high fluorescence intensity, corresponding to a positive ethanol composition gradient. For ethanol gradient in the configuration of three zones in Figure 2.3A, several assumptions are made: (a) At the boundary between zone 2 and 3, the ethanol mass fraction on the side of zone 3 is assumed to be equal to the composition of the octanol-rich subphase immediately after being formed by phase separation ($w_{eth23,3}$). (b) At the boundary of zone 1 and 2, the ethanol composition on the side of zone 2 is assumed to be the same as the saturated water-rich subphase from phase separation ($w_{eth12,2}$). (c) From the boundary between zones 2 and 3, the ethanol fraction in the liquid in zone 2 ($w_{eth23,2}$) is proportional to the fluorescence intensity ($I_{12,2}$) and composition from zone 2 at the

boundary location between 1 and 2 ($x_{eth12,2}$). For 30% octanol in solution A, $w_{eth23,3}$ is estimated to be 0.375 and $w_{eth12,2}$ to be 0.326, based on UNIFAC equilibrium calculations [23]. Linear interpolation for assumption (c) yields an expression for the ethanol mass fraction as a function of fluorescence intensity:

$$w_{eth23,2} = w_{eth12,2} \times I_{23,2}/I_{12,2} \tag{2.4}$$

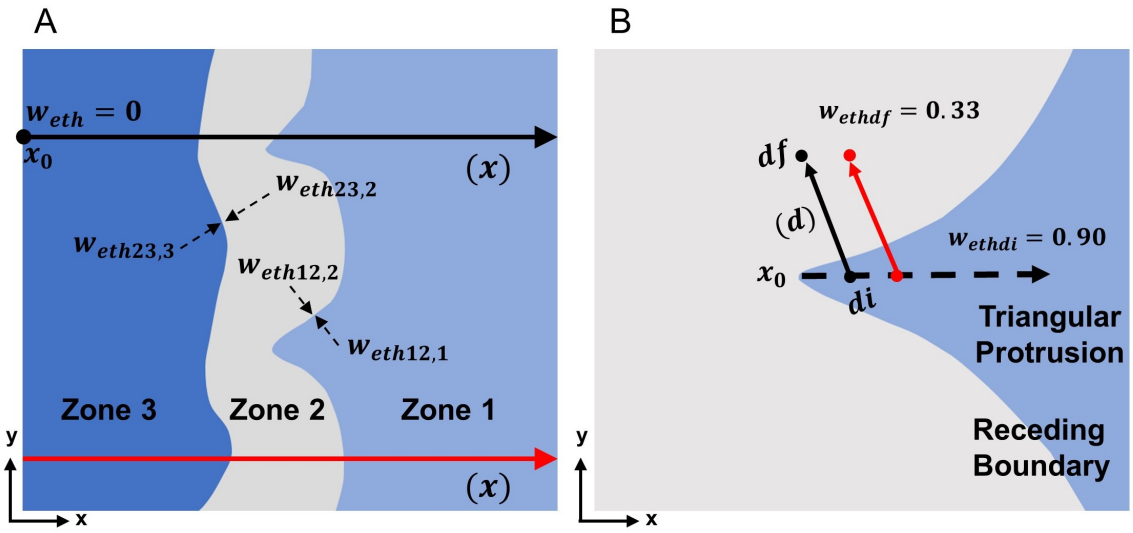

Figure 2.3: Fluorescence intensity characterization for two configurations of the liquid mixtures. (A) Fluorescence intensity values were taken as a function of x-direction. The two horizontal lines illustrate intensity data as a function of x-position at two y-values. At x_0 the ethanol fraction (w_{eth}) is taken to be 0. Ethanol fraction at each boundary location is labelled with zone numbers. $w_{eth12,1}$ represents ethanol mass fraction at boundary between zone 1 and 2 from zone 1 side. $w_{eth12,1}$ has solution A ethanol composition, $w_{eth12,2}$ water-rich phase composition, $w_{eth23,3}$ oil-rich phase composition. (B) Fluorescence intensity values taken as function of position (d) on parallel lines along the x-direction within and adjacent a triangular feature on a boundary. di and df are the initial and final positions of intensity measurements with ethanol fraction w_{ethdi} and w_{wthdf}. Fluorescence intensity measurements at a triangular feature start from the tip location at x_0 and continue towards the positive x-direction.

Composition gradients were evaluated in the boundary region, in a coarse-grained manner, as illustrated in Figure 2.3A, and in a more fine-grained manner, within and adjacent to key features on a boundary, as illustrated in Figure 2.3B. Coarse-grained gradients were obtained from fluorescence intensity profiles of the ethanol

mass fraction (w_{eth}) along the x-direction (x) at a fixed time and fixed y values. Tables of intensity values ($I(x)|_{y,t}$) were normalized using the intensity at the side channel position (I_{x0}) as $I(x)/I_{x0}$. The normalized intensity data contained significant image-related noise, which was reduced using a Savitzky-Golay filter in MATLAB.

Fine-grained gradients, used to evaluate the effect of diffusive boundary shape on the mobility of droplets, were obtained by taking the intensity profile along fixed lines perpendicular to local features of the diffusive boundary between solution A and B. The data acquisition process is illustrated in Figure 2.3B, where the boundary has a triangular feature. The normalized intensity profile (I_{norm}), as a function of position (d) across the boundary region, was fit to a Gaussian decay model:

$$I_{norm}(d) = \frac{I(d) - I_{df}}{I_{di} - I_{df}} \sim \exp(-\frac{d^2}{a(x)|_t}) \tag{2.5}$$

where $I(d)$, I_{di}, and I_{df} are the mean gray values at position d along the diffusive boundary, the initial position at the center of the mixing zone and the final position at the water-rich side, respectively. The model parameter $a(x)|_t$, was fitted to $I_{norm}(d)$ profiles using least squares regression. $a(x)|_t$ values were used to illustrate the difference in sharpness of intensity profiles with x-position at a fixed time. Normalized intensity values were converted to ethanol mass fraction profiles with the boundary conditions of the water-rich phase $w_{eth}(I_{df})$ and the initial solution A composition $w_{eth}(I_{di})$.

Chapter 3

Enhanced displacement of phase separating liquid mixtures in 2D confined spaces[1]

3.1 Composition regimes

The phase diagram for the model ternary mixture 1-octanol (oil), ethanol (good solvent) and water (poor solvent) is illustrated in Figure 3.1A. Confined liquid compositions labelled from 1 to 11 (Table 2.1), are shown in the phase diagram. The phase boundary was adapted from the literature [92], tie lines not shown were computed using the UNIFAC model and inform the discussion. The Dortmund UNIFAC model was implemented using the parameter values noted in Appendix B.

The mixing between solution A and water as water diffused into the narrow channel induced liquid-liquid phase separation. Below we show the displacement process along with phase separation for the wide range of solution A compositions listed in Table 2.1. The 1-octanol-rich liquid is revealed using a hydrophobic dye in fluorescence images. The displacement dynamics are categorized into four regimes, as shown in Figure 3.1B-E.

[1] This chapter presents the results and discussion of work published as G. F. Arends, J. B. You, J. M. Shaw, X. Zhang. Enhanced displacement of phase separating liquid mixtures in 2D confined spaces, Energy & Fuels. 35 (2021) 5194–5205.

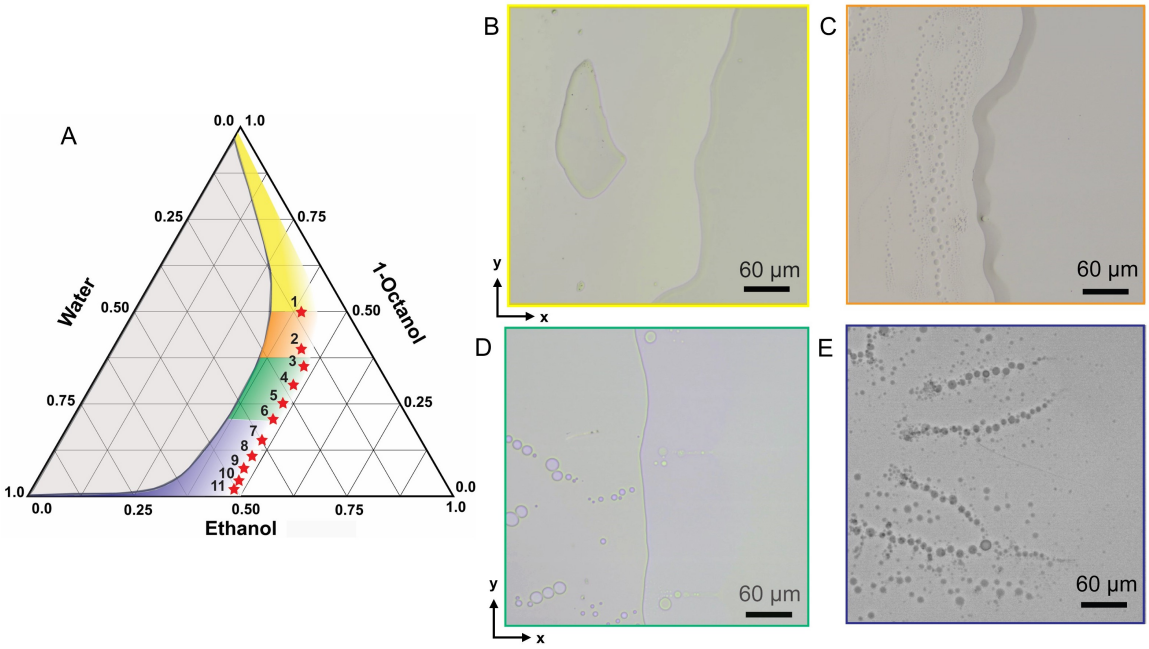

Figure 3.1: Overview of different dynamic regimes. (A) Ternary phase diagram of 1-octanol, ethanol, and water system in terms of mass fractions with evaluated experimental compositions annotated. Displacement regimes are indicated by colors: Regime 1 (yellow), Regime 2 (orange), Regime 3 (green), and Regime 4 (blue). Adapted from *ACS Cent. Sci.* **2016**, 2, 7, 467–475 [92]. (B-E) Representative optical images of the phase separation regimes are shown in colour-coded rectangles as in (A).

3.2 Regime 1: Receding interface

Regime 1 corresponds to a high 1-octanol concentration, above 50% by mass in solution A. The composition is labelled in the phase diagram in Figure 3.2A. As water diffused from the side channel, the resulting images in Figure 3.2B show a clear interface separating solution A from water in the narrow channel.

A few 1-octanol microdomains pinched off from the receding phase boundary at several locations and remained attached to the hydrophobic wall on the water side of the boundary. Their composition was confirmed using fluorescence imaging (Figure 3.2C). This fluorescence image of a representative domain formed from solution A doped with an oil-soluble fluorescent dye (Nile red). The high fluorescence intensity

from the microdomain indicates the high concentration of the dye in the microdomain, in contrast to the absence of a fluorescence signal from the surrounding liquid. The spatial distribution of the dye is consistent with the chemical composition of the 1-octanol-rich microdomains surrounded by water-rich liquid.

In this regime, water diffusing into the narrow channel did not lead to liquid-liquid phase separation along the boundary - behaviour consistent with that of an immiscible displacing liquid. However, liquid-liquid phase separation did occur within the stranded microdomains. Many nanodroplets (with a diameter of approximately 4 μm) formed, as shown in Figure 3.2D. The formation of these water-rich nanodroplets is attributed to subphase formation arising from the diffusion of water into the microdomains followed by liquid-liquid phase separation.

As water diffuses into a microdomain and 1-octanol and ethanol diffuse out, the global composition of the microdomain changes. To a first approximation, the dilution path that is followed is indicated by the dashed line in the phase diagram in Figure 3.2A. The mixture becomes unstable as the composition intersects the solubility curve and spontaneously forms water-rich and 1-octanol-rich subphases. Although the global composition of the microdomain at separation is unknown, the compositions of the 1-octanol-rich and water-rich subphases created are approximately 80 and 19% 1-octanol by mass. It is interesting that phase separation occurred in the microdomains of stranded solution A, but not at the boundary between water and solution A. The large surface to volume ratio of the small microdomains permits them to become supersaturated with water quickly. By contrast, at the boundary, water diffuses into the bulk 1-octanol-rich phase, and 1-octanol and ethanol diffuse into the bulk water-rich phase. Consequently, the liquids on both sides of the boundary do not supersaturate within the time frame of measurements. At longer times, one would certainly expect the microdomains to dissolve into the water-rich phase.

While the shape and size of stranded solution A microdomains varied between experiments (Figure 3.2D), possibly due to the nature of the interface instability -

subphase formation within them over time was common.

If we now focus on the displacement of the boundary between solution A and water, in the absence of microdomain formation, we can see that the x-location displacement rate is essentially time-invariant with an average value of $10.7 \pm 0.3\ \mu m/s$ (Figure 3.2E). Figure 3.2F shows the fluctuating x-location displacement rate where microdomains form and detach over time. The interface progressively displaced solution A in the positive x-direction. During the formation of a microdomain, the interface remains stationary or moves backward. When a microdomain detaches from the interface, the interface accelerates in the positive x-direction. Such cycles were observed at multiple locations on the surface.

The blue and red dashed curves in Figure 3.2F are 1D diffusion-based displacement curves, $l = (2Dt)^{1/2}$, fitted to the interface displacement data before microdomain detachment to obtain an effective diffusion constant [43]. The effective diffusivity varies as the boundary progresses. The values range from $5.3 \times 10^{-9}\ m^2/s$ for a part of the boundary without microdomain formation (Figure 3.2E) and 2.8×10^{-10} to $7.9 \times 10^{-10}\ m^2/s$ for a location where there is microdomain formation. The mutual diffusivities of water and ethanol, and water and octanol range from 1.08×10^{-10} to $1.23 \times 10^{-9}\ m^2/s$ and 2.0×10^{-10} to $7.3 \times 10^{-10}\ m^2/s$, respectively [93–95]. So the diffusion rates are consistent with expectations. In locations with microdomain formation, the boundary displacement rate was variable and ranged from 4.3 to 14.0 $\mu m/s$.

The influence of solution A microdomains on the local motion of the boundary may be attributed to the pinning effect and mass transfer to microdomains. Imperfections on the wall surface pin the boundary, leading to microdomain formation once the boundary becomes unstable. As the microdomain is formed, the water-rich phase close to the microdomain experiences interfacial tension opposite to its flow direction. The acceleration experienced after the detachment of the microdomain may be attributed to the release of built-up tension that comes from the stretched interface

of the microdomain.

In Regime 1, water largely displaces solution A (with a high initial concentration of 1-octanol) in a confined space with one hydrophobic wall. The large-scale stability of the boundary between solution A and water contributes to the effective displacement. In contrast, local instability of the boundary and microdomain formation leads to lower and fluctuating displacement rates indicated in Figure 3.2F, as well as less efficient 1-octanol-rich liquid displacement.

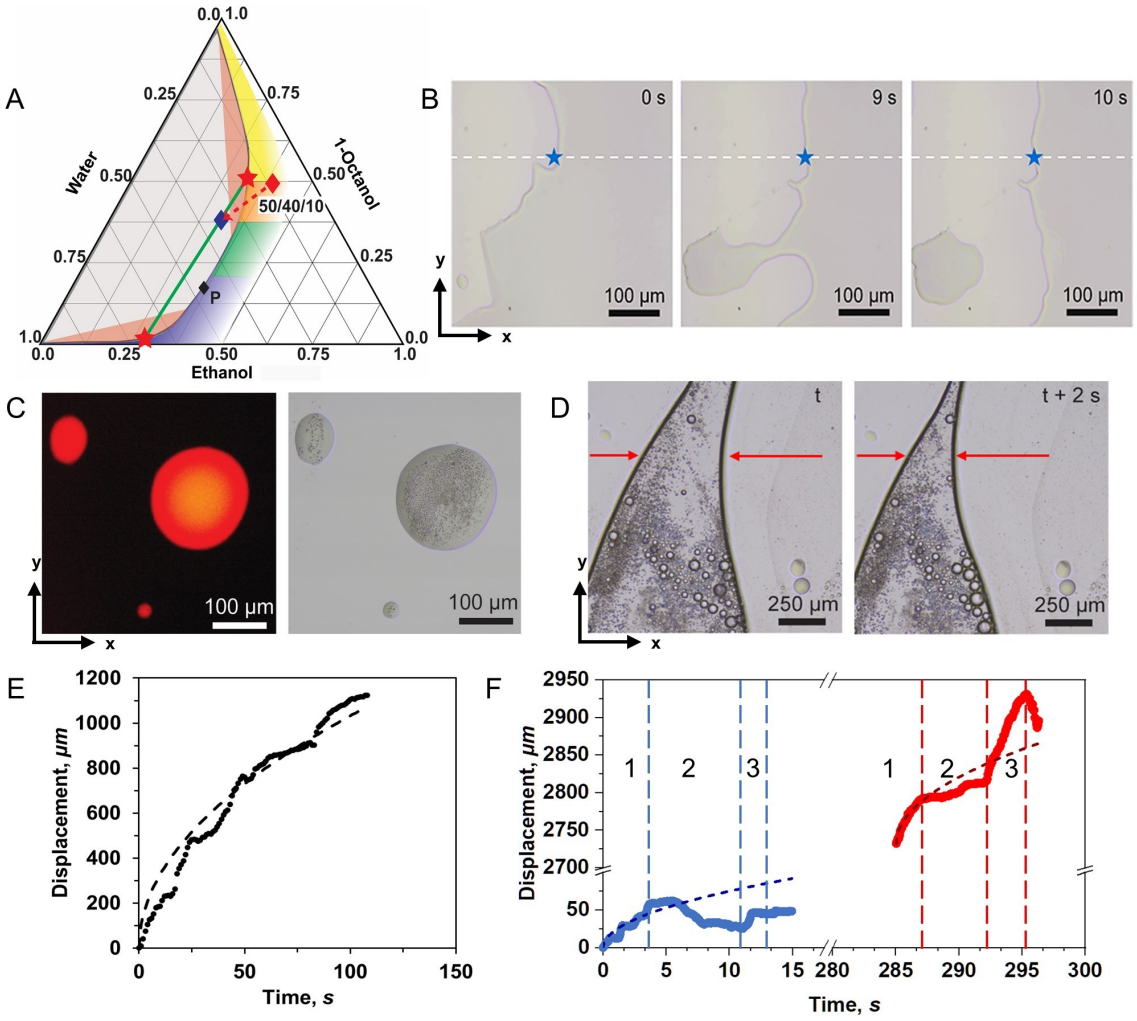

Figure 3.2: Overview of Regime 1. (A) Ternary phase diagram indicating the dilution path with the two macroscopic subphases formed. P is the plait point of the ternary mixture. Red regions within the phase envelope are the Ouzo and reverse Ouzo regions. The initial solution A composition is given by a red diamond. An illustrative unstable mixture composition during dilution is given as a blue diamond. The red stars represent the 1-octanol-rich and water-rich compositions formed along the green tie line. Adapted from *ACS Cent. Sci.* **2016**, 2, 7, 467–475 [92]. (B) Time-based optical images of early film and domain development. (C) Side by side fluorescence and bright-field images of representative microdomains. (D) Time-based images of a deformed domain narrowing with time. (E) Plot showing local boundary displacement without microdomain formation. (F) Plot showing local boundary displacement at a location where microdomains form. Blue data set was taken along the x-direction indicated by the white dashed line in (B) with the same reference position of the side channel. Time window 1 is for a period without a microdomain present. During time period 2, a microdomain forms at the boundary. Time period 3 starts as soon as the microdomain detaches from the boundary. The formation of microdomains slows boundary displacement. Their detachment accelerates boundary displacement. Red data set was taken after 270 *s* at same y-location of blue data set.

3.3 Regime 2: Moving microdroplet zone

Regime 2 corresponds to intermediate 1-octanol concentrations, about 40% by mass in solution A. The overall behaviour in Regime 2 differs markedly from Regime 1, despite the similarity of the solution A compositions. Starting from this composition, the subphase formed by mixing with water is well approximated by the trajectory shown in Figure 3.3A. From the tie line shown in the phase diagram, much more 1-octanol-rich subphase is still expected than water-rich subphase following liquid-liquid phase separation. Unlike Regime 1, a mobile 1-octanol-rich microdroplet zone separates solution A and water throughout the narrow channel, as shown in the fluorescence images in Figure 3.3B. A dark zone containing water, a zone rich in microdroplets and a clear zone of solution A are clearly present.

Figure 3.3C shows the level of fluorescence intensity crossing the three zones. The high fluorescence intensity in the intermediate zone confirms that it is rich in 1-octanol. The boundary zone appears dark in bright field images, possibly due to scattering from small 1-octanol-rich drops.

The time-based images in Figure 3.3D show oscillation of the boundary zone, but this oscillation does not lead to the formation of stranded microdomains. Instead, the boundary zone thickness appears to remain constant at 18-20 μm in the time interval of 12 s as the boundary moves forward, as shown in the high magnification inset (Figure 3.3D). The time invariance of the boundary zone thickness may indicate that the mass transfer occurring through the boundary is balanced, even though the compositions of the water-rich and 1-octanol-rich phases in the zone vary along the x-direction.

Lines of stranded 1-octanol-rich droplets form behind the receding boundary zone, mirroring the shape of the boundary as it progresses (Figure 3.3E). The interval between two lines of droplets on the surface may be related to the time required for phase separation to occur in the boundary zone or the time required for the droplets

inside the boundary zone to accumulate on the contact line with water.

The boundary displacement rate is quantified in Figure 3.3F along a fixed-line in the x-direction. The rate of displacement fluctuates with time due to the oscillatory advancement of the boundary zone. Again, the data can be fitted with a diffusion model [43]. Compared to the displacement of the boundary in Regime 1 (for a case where microdomain formation does not occur), the displacement versus square root of time is slower in Regime 2. This is evidenced by the lower effective diffusivity obtained from the fit, which ranged from 5.8 $\times 10^{-10}$ to 6.7 $\times 10^{-10}$ m^2/s, and a lower displacement rate of 5.8 $\mu m/s$.

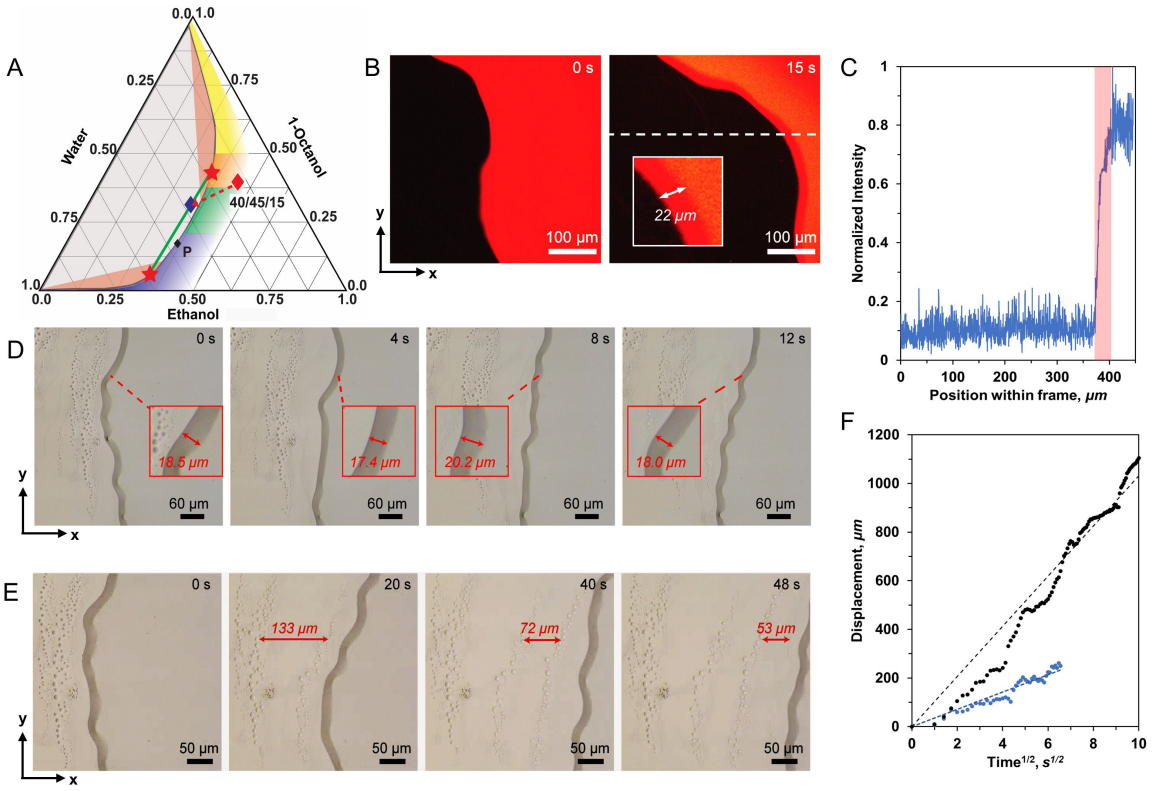

Figure 3.3: Overview of Regime 2 boundary displacement dynamics. (A) Ternary phase diagram indicating the approximate dilution path and the compositions of the subphases formed. P is the plait point of the ternary mixture. Red regions within the phase envelope are the Ouzo and reverse Ouzo regions. The initial solution composition is given by a red diamond. The unstable mixture composition after dilution is approximated by a blue diamond. The red stars represent the 1-octanol-rich and water-rich subphases that are formed based on the green tie line. Adapted from *ACS Cent. Sci.* **2016**, 2, 7, 467–475 [92]. (B) Time-based fluorescence imagery at 40% 1-octanol within Regime 2. (C) Normalized fluorescence intensity as a function of x-location within the frame of (B) at t = 15 s. The red area in the graph indicates a boundary zone. (D) Time-based optical images of moving boundary within Regime 2 with an initial solution A composition of 40% 1-octanol. The inset contains magnified images of the moving boundary indicating zone thickness. (E) Time-based optical images of droplet formation in the boundary zone. (F) Boundary displacement as a function of the square root of time assuming diffusion-based dynamics. Regime 1 smooth interface displacement (black) and Regime 2 (blue) comparison.

3.4 Regime 3: Moving three-zone configuration

Regime 3 arises for the 1-octanol concentration range 20% to 30% by mass in solution A. Data for the 30% case are presented in detail and are representative of this regime. Figure 3.4A illustrates the dilution process within the phase diagram. On separation, approximately equal amounts of water-rich and 1-octanol-rich subphases form because the dilution line intersects the phase envelope close to the plait point.

Fluorescence images in Figure 3.4B reveal three distinct zones along the x-direction as labelled in Figure 3.4B at t = 30 s. The normalized fluorescence intensity plotted in Figure 3.4C shows that zone 1 consists of a 1-octanol-rich phase revealed by the partition of a dye [44], that zone 2 consists of a water-rich subphase, and that zone 3 contain numerous immiscible water-rich droplets (dark features in fluorescence images within a 1-octanol-rich phase).

Figure 3.4D illustrates the early development of the three-zone configuration as water enters from the side to the narrow channel. A 1-octanol-rich phase forms from phase separation and water droplets appear simultaneously within the 1-octanol-rich subphase and later coalesce and merge into a water-rich zone 2.

The displacement of solution A proceeds as the entire zone 2 moves into the narrow channel. The width of zone 2 appears to increase slightly with time at a fixed y-position, as shown in Figure 3.4E. The most noticeable aspect of the entire zone 2 is its stability in space over minute-long time scales. We suspect that this stability is related to the near-constant width of zone 2, which we in turn attribute to the near equivalence of the influx and outflux of liquid to zone 2 over time. The liquid may enter zone 2 in the form of water-rich droplets from zone 3 or by water entering from the side channel, as evidenced in the Figure A.1. Concurrently the 1-octanol-rich liquid leaves zone 2 to zone 3. The balancing of mass fluxes in and out of zone 2 accounts for its stability.

The displacement of zone 1 to zone 2 and zone 2 to zone 3 boundaries versus the

square root of time are shown in Figure 3.4F. These boundaries move with an oscillatory behaviour in the positive x-direction with a slower overall rate than the previous regime 2 at 0.71 $\mu m/s$. The fluctuations were found to be related to the water-rich droplets entering zone 2. At locations where droplets merged with the boundary between zone 2 and 3, the boundary retracted in the negative x-direction. The boundary successively becomes deformed, leading to the acceleration of the boundary in the positive x-direction as the shape of the boundary starts to recover. The boundary displacement curves from the two locations in Figure 3.4F show similar trends in pinning and depinning transitions. Regardless of all the fluctuations in boundary motion, the three-zone configuration remained stable with time due to water replenishment.

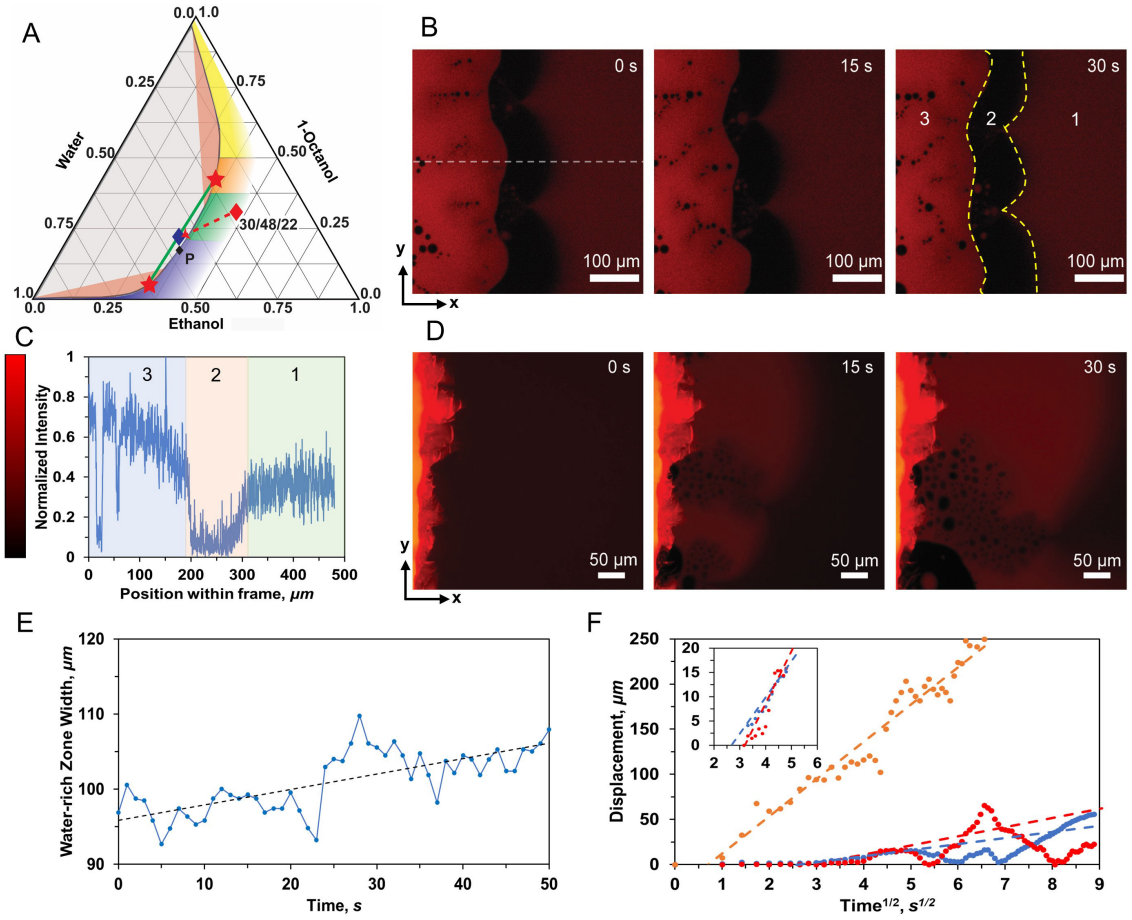

Figure 3.4: Overview of Regime 3 and dynamic data for 30% 1-octanol in solution A. (A) Ternary phase diagram showing the approximate dilution path and subphases compositions. P is the plait point of the ternary mixture. Adapted from *ACS Cent. Sci.* **2016**, 2, 7, 467–475 [92]. (B) Illustrative time-based fluorescence images for Regime 3. Zone 1 is a 1-octanol-rich phase, zone 2 is a water-rich phase, and zone 3 is 1-octanol-rich liquid with dispersed water-rich phase drops. (C) Normalized fluorescence intensity as a function of x-location within the frame of (B) at t = 0 s. (D) Time-based fluorescence images directly after water enters the narrow channel. (E) Water-rich zone 2 widths as a function of time (dashed line indicating slight increasing trend). (F) Boundary displacement as a function of the square root of time illustrating diffusion-dominated movement. (Blue) corresponds to the boundary between zones 1 and 2. (Red) corresponds to the boundary between zones 2 and 3. (Orange) corresponds to Regime 2 displacement data. Inset depicts the slopes, from $2 < t^{1/2} < 6$ for the boundaries in Regime 3.

3.5 Regime 4: Diffusive boundary

In Regime 4, the composition ranges from 2-20% 1-octanol by mass in solution A. In this regime, a diffusive boundary forms and the dynamics differ from the other three regimes. The results depicted in Figure 3.5 are for 10% 1-octanol by mass.

Figure 3.5A shows the approximate dilution path and subphase compositions in the phase diagram for the 10% 1-octanol case. The diluting mixture intersects the phase envelope below the plait point, and following phase separation, the water-rich subphase fraction is expected to be an order of magnitude greater than the 1-octanol-rich subphase mass fraction.

Figure 3.5B shows the diffusive boundary at an early transition stage consisting of numerous triangular protrusions of solution A that extend into the water phase. Droplets formed from the tips of these protrusions in the water-rich phase were larger than those formed at other positions along the boundary because, at the tip of the protrusions, the concentration gradients are sharper than at other positions [38, 43]. At longer times, protrusions approach one another and collapse into a line-shaped boundary region, as shown in Figure 3.5C. At longer times, droplets are formed along the entire boundary in the water-rich phase.

Fluorescence images in Figure 3.5(D, E) show the 1-octanol-rich protrusions with a 1-octanol concentration greater than in solution A. Ethanol transfers preferentially to the water-rich phase. After 30 seconds, the composition of the protrusions becomes consistent with that of the 1-octanol rich droplets formed, as indicated by the fluorescence intensity.

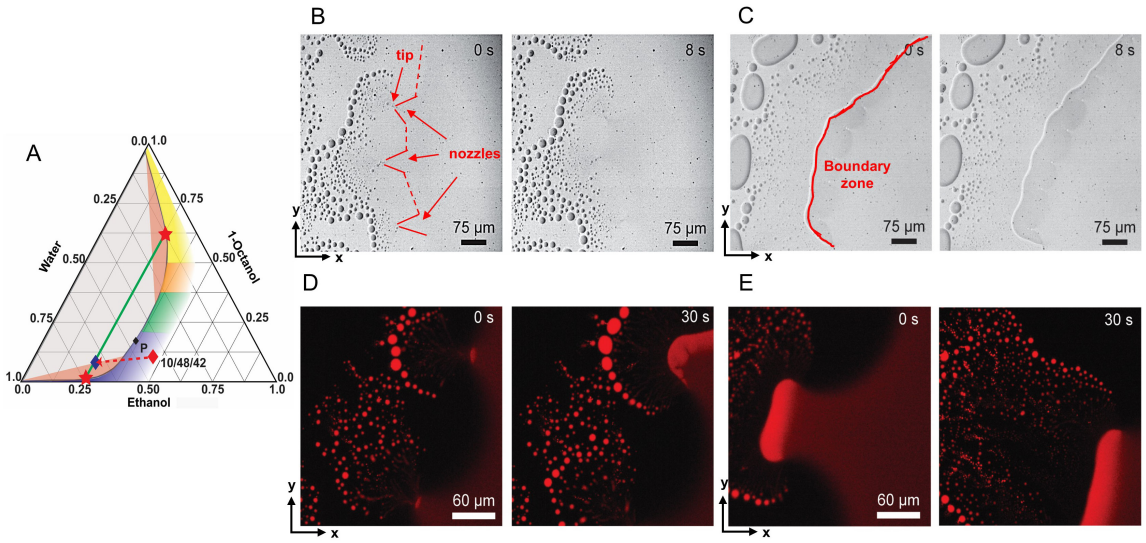

Figure 3.5: Overview of Regime 4 at low 1-octanol compositions. (A) Ternary phase diagram indicating the approximate dilution path and subphase compositions. P is the plait point of the ternary mixture. Adapted from *ACS Cent. Sci.* **2016**, 2, 7, 467–475 [92]. (B) Time-based optical images showing boundary development and (C) boundary for the 10% 1-octanol solution A case. (D) Time-based fluorescence imagery of protrusion and change to (E) line-shaped boundary for the 10% 1-octanol case.

Figure 3.6A provides an overview and dynamic data for solution A with 2% 1-octanol. Figure 3.6A shows the approximate dilution path and subphase compositions. The mass ratio of water-rich to 1-octanol-rich subphase is expected to be around 25 to 1 in this case. Fluorescence images in Figure 3.6C again show triangular protrusions of 1-octanol-rich liquid into the boundary. While the outcomes are similar to those described in Figure 3.5, the triangular protrusions are more stable (Figure 3.6B). This outcome is consistent with earlier work showing that droplets form branches from a diffusion-limited nucleation and growth process in a 2D confinement at low concentration [46].

Once formed, numerous droplets travelled toward the side channels in the negative x-direction before becoming immobilized on the wall surface or coalescing with other droplets. The lines with low fluorescent intensity indicated in the yellow boxes in Figure 3.6C show induced droplet flow. The droplets appear as lines due to the

exposure time of the camera when taking fluorescence imagery. This induced flow may explain the relatively fast boundary displacement rate associated with Regime 4.

The optical images in Figure 3.6D and E indicate the qualitative similarity of droplet formation and boundary movement phenomena for 5% and 8% 1-octanol by mass in solution A. Differences arise from the number of droplets formed and droplet size with time.

The displacement of the boundary is plotted against the square root of time for the 2%, 5% and 10% initial 1-octanol wt-% cases. As indicated by the slopes added to each curve in Figure 3.6F, a slower followed by a more rapid diffusive displacement process is clearly evident for the 2% and 10% conditions. While qualitatively similar, the first diffusion-controlled process slows and has a longer duration as the initial 1-octanol wt-% increases. In Regime 4, boundary displacement is faster than Regime 3 compositions, and there are seldom oscillations in displacement versus time plots.

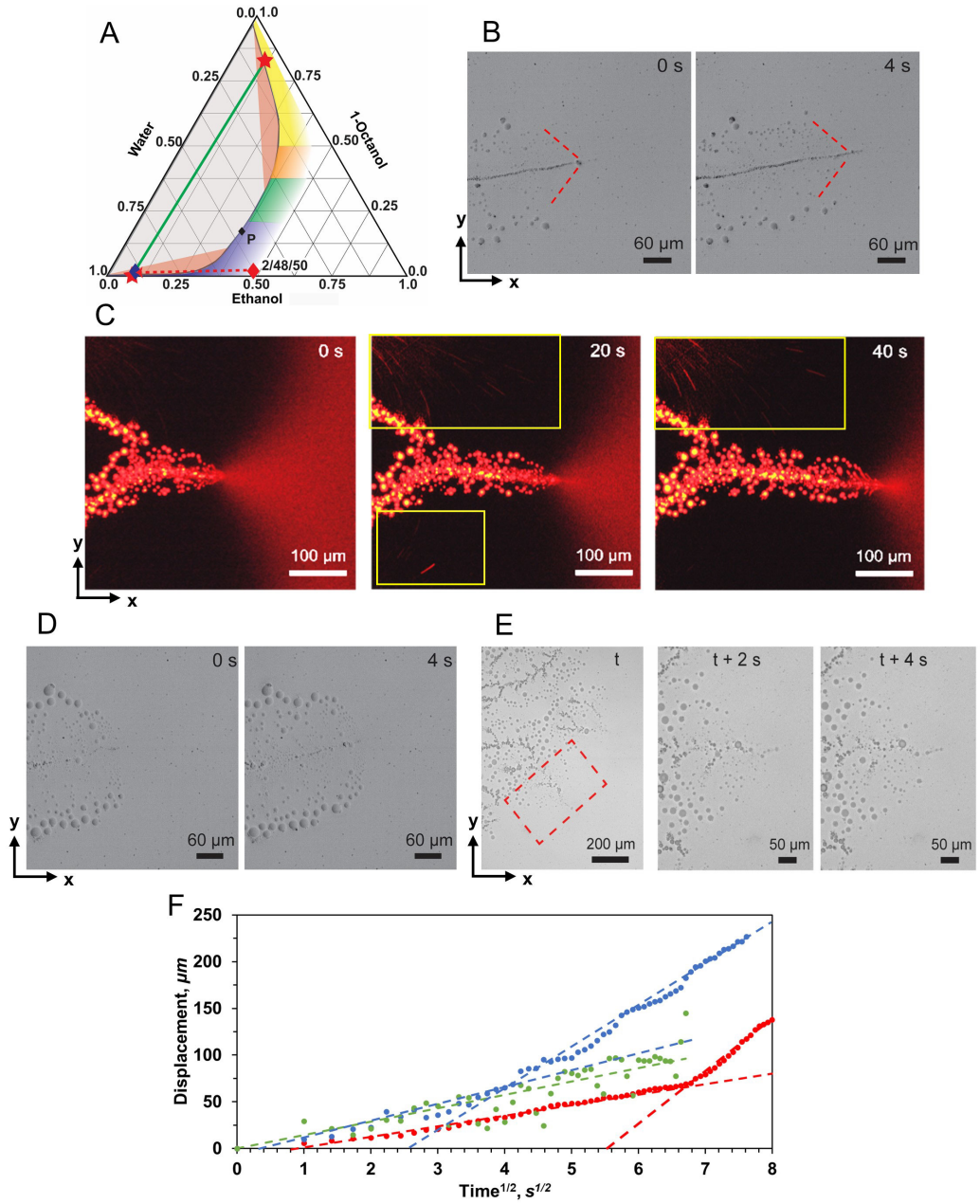

Figure 3.6: Regime 4 dynamics with a focus on low 1-octanol wt% compositions. (A) Ternary phase diagram indicating approximate dilution path and subphase compositions for solution A with an initial 1-octanol composition of 2% by mass. Adapted from *ACS Cent. Sci.* **2016**, 2, 7, 467–475 [92]. (B) Time-based optical images of triangular-shaped boundary movement using 2% by mass in solution A. (C) Time-based fluorescence images of 2% 1-octanol by mass indicating the 1-octanol-rich and water-rich regions. Yellow boxes show droplets recirculating back to the boundary region. Time-based optical images comparing the 5% 1-octanol (D) and 8% 1-octanol (E) conditions. (F) Boundary displacement as a function of the square root of time plot comparing the 2% octanol (blue), 5% (green) and 10% (red) conditions. Dashed lines show anticipated two-tiered diffusion-based displacement dynamics.

3.6 Comparison of the displacement rates in four regimes

In Figure 3.7A, we compare the displacement rates in all four regimes presented. An effective diffusivity was calculated for each regime, as shown in Figure 3.7B. The highest effective diffusivity value was obtained in Regime 1 at 50% of 1-octanol for a smooth boundary, which has an enhanced effective diffusivity of $8 \times 10^{-9}\ m^2/s$. The effective diffusivity obtained is thus higher than the expected range of the mutual diffusivities between water and ethanol (1.1×10^{-10} to $1.2 \times 10^{-9}\ m^2/s$), and water and 1-octanol (2.0×10^{-10} to $7.3 \times 10^{-10}\ m^2/s$) showing the enhanced diffusion. In both high and low 1-octanol ratios of Regimes 1 and 4, the displacement rate of the boundary was faster at $\sim 15\ \mu m/s$ and $\sim 4\ \mu m/s$. In contrast, in the intermediate Regime 3, the rate is only $\sim 0.7\ \mu m/s$ as shown by the average velocities in Figure 3.7C. Boundary displacement in Regime 3 is slower than in the other regimes but remains 2 times the displacement rate expected for a purely diffusive single-phase process obtained from the effective diffusivity.

To understand the dependence of displacement rate on 1-octanol concentration, including a shallow minimum at intermediate 1-octanol concentrations, we must consider competing effects. Differences in the energy released during phase separation with 1-octanol concentration are illustrated in Figure 3.7D. The energy released during the transition from a non-equilibrium single-phase state to an equilibrium two-phase state increases with 1-octanol concentration. To the extent that displacement rate depends on this thermodynamic driving force, one would anticipate an increase in displacement rate with 1-octanol concentration. This effect is clearly evident at high 1-octanol concentration. However, the displacement rate at low 1-octanol concentrations is somewhat higher than at intermediate 1-octanol concentrations. We attribute this apparent enhancement in displacement at low 1-octanol concentrations to droplet propulsion and the flow induced in the continuous phase from the self-

propelling microdroplets in this concentration range, i.e., to how the energy of phase transition is dissipated.

Impacts of relative viscosity of the liquid phases, and the relative wettability of the liquid phases on the wall surface, which approach one at intermediate 1-octanol concentrations (near the plait point), are seen as secondary. Viewed from this perspective, the strong dependence of displacement rate on the initial composition is expected to be a general feature for displacing multi-component liquids undergoing phase separation. Further, compositions transitioning through Regimes 1 and 2 are preferred for displacing liquid, while compositions transitioning through Regimes 3 and 4 are preferred for promoting the separation and extraction of a component or a component category (1-octanol a model oil in this case) from the solution at lower overall displacement rates.

We note that the 1-octanol/ethanol/water chemical system is complex, and there has been extensive study on how chemical composition affects the molecular level structures of single-phase solutions near the phase envelope [41, 92, 96–98]. Compared to the work by Lopian et al., in our Regime 1, the initial compositions correspond to a reverse aggregate regime in their work. Regime 2 compositions would be those transitioning from the reverse aggregate to the bicontinuous regime. Regime 3 would be within the bicontinuous regime, and Regime 4 would be considered the pre-Ouzo compositions. However, we could not directly link the displacement rate to the structures of microemulsions in space and in time. The reason is that the structures of microemulsions are on a molecular level scale, whereas our experimental observations are on a much larger scale (at least from 250 nm to 1 μm) due to the limitation of the spatial resolution.

The impacts of high ethanol content in the initial solution A are not studied in this work. We expect a high initial ethanol content to result in a composition path close to the axis from ethanol to water within the phase diagram. The reason is that the diffusive mixing may not generate enough concentration gradient for 1-octanol to

form droplets. Therefore, no dynamic events due to phase separation may take place.

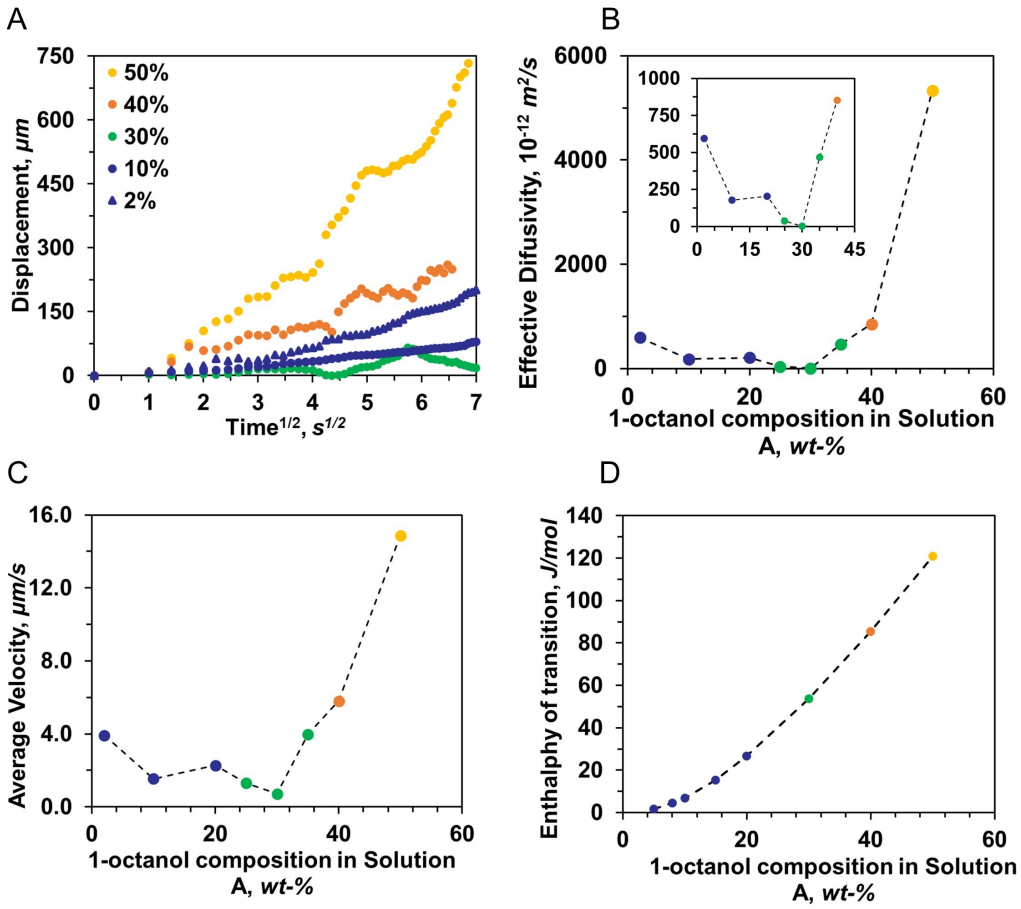

Figure 3.7: (A) Summary of displacement versus square root of time for 1-octanol compositions spanning the four regimes. (B) Effective diffusivity and average velocity (C) calculated from displacement versus time data in all four regimes. (D) Calculated enthalpy of transition from a non-equilibrium single-phase state to two equilibrium states based on the Dortmund UNIFAC method.

3.7 Using water + ethanol binary mixtures to displace solution A

Additional experiments were performed at high and low 1-octanol composition regime conditions using a displacing liquid containing 25% ethanol by mass in water. Figure 3.8A shows the approximate trajectory and associated tie line from the dilution process with this displacing liquid for a Regime 1 composition when water alone is

used to displace it (see E1 in Table 2.2). The resulting water-rich phase formed by phase separation, in this case, has a composition corresponding to a Regime 4 solution composition, while the composition of the 1-octanol-rich phase remains qualitatively similar.

Figure 3.8B shows an observed insoluble moving boundary and stranded 1-octanol-rich microdomains similar to the Regime 1 behaviour (Figure 3.2B) with fewer undulations. The smoother boundary displacement may be attributed to the reduction in the interfacial tensions and the pinning effect from the substrate with ethanol in the displacing liquid. Higher solubility of 1-octanol in ethanol solution may attribute to smaller microdomains.

Consistent results were also observed in Figure 3.8C, where solution A was 10% 1-octanol by mass, and the displacing liquid was 25% ethanol by mass solution (see E4 in Table 2.2). In this case, droplets formed behind the moving boundary and dissolved slowly due to the high solubility of 1-octanol in displacing liquid.

The boundary displacement as a function of time summarized in Figure 3.8D shows a time-invariant displacement rate for binary displacing liquid. For conditions with water as the displacing liquid, the boundary displacement rate for Regime 4 is 10 times greater, and for Regime 1, the rate is 0.9 times lower. The faster displacement rate for Regime 1 may be attributed to improvements in solubility of 1-octanol in the displacing liquid.

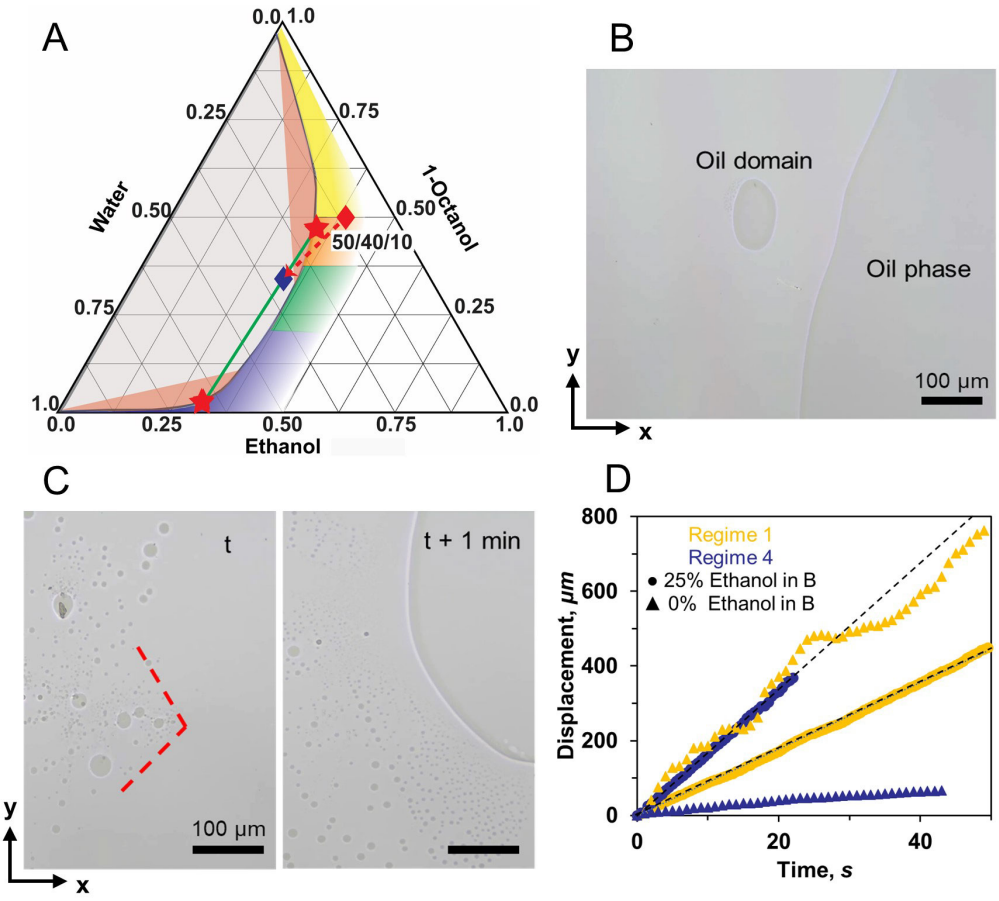

Figure 3.8: (A) Ternary phase diagram indicating the approximate dilution path using 25% ethanol in the displacing liquid at Regime 1 condition. Adapted from *ACS Cent. Sci.* **2016**, 2, 7, 467–475 [92]. (B) Optical image of Regime 1 condition using 25% ethanol by mass in the displacing liquid. (C) Time-based optical images of Regime 4 condition using 25% ethanol by mass in the displacing liquid. (D) Boundary displacement as a function time for 25% ethanol in displacing liquid comparing the 10% 1-octanol (blue) and 50% (yellow) conditions. Dashed lines indicate linear regression from data. Data for water (0% ethanol) as displacing liquid in both regimes was added for comparison (triangles).

3.8 Displacing water with solution A

By displacing water with solution A (a 1-octanol-containing ternary mixture), we are able to consider the impacts of reverse flow arising in large-scale porous media and to understand the impacts of relative wettability of the displacing liquid. Two cases, linked to experiments described in detail above, are illustrative.

Figure 3.8A shows the insoluble boundary arising when the confined liquid is water and the displacing liquid is solution A. The solution A composition corresponds to Regime 1 (see R1 in Table 2.2) shown in Figure 3.2A. Droplets did not form within microdomains left behind by the boundary. Instead, small 1-octanol droplets were confined in the boundary zone, similar to Regime 2 conditions in Figure 3.3. The boundary displacement rate was 9 times faster compared to normal Regime 1 conditions.

Figure 3.9B shows the displacement boundary when solution A composition corresponds to Regime 4 (see R4 in Table 2.2). In this case, 1-octanol-rich droplets and domains form at the boundary . The overall displacement rate of the boundary (Figure 3.9C) is time-invariant (77 $\mu m/s$) and 50 times faster than normal Regime 4 conditions. This dramatic difference in displacement rate demonstrates that using displacing liquids with better wettability (lower interfacial tension) on the wall surface may provide an effective route to enhance fluid displacement rate in confinement. Such wettability manipulation is a common professional practice for enhanced oil recovery [21].

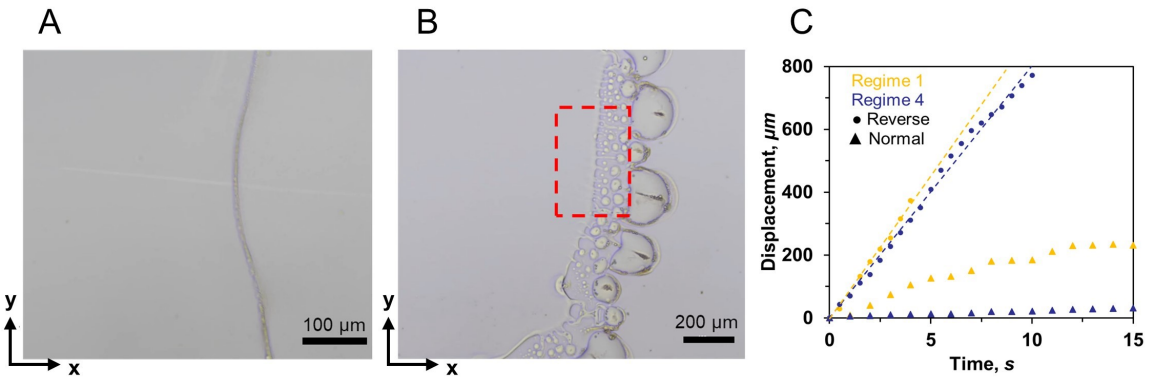

Figure 3.9: (A) Optical image showing confined water being displaced by solution A with a 50% 1-octanol by weight composition. (B) Optical image showing confined water being displaced by solution A with a 10% 1-octanol by weight composition. (C) Boundary displacement as a function time for reverse conditions comparing the 10% octanol (blue) and 50% (yellow) conditions. Dashed lines indicate linear regression of data. Data for normal conditions with water as displacing liquid and ternary solution as the confined liquid in both regimes is added for comparison (triangles).

3.9 Conclusion

We investigate the displacement process for phase-separating ternary liquid mixtures in 2D confinement. The model mixtures contain 1-octanol (a model oil), water (a model poor solvent) and ethanol (a model good solvent), where water (the poor solvent) is the displacing fluid. One of the confining walls is hydrophobic, and the other is hydrophilic. Four composition-dependent displacement regimes are identified. While the details of the displacement mechanism corresponding to each regime differ, order of magnitude enhancements over single-phase diffusive displacement arise. The displacement rate was also shown to be further enhanced with the addition of ethanol (good solvent) to the displacing liquid, improving the wettability on the wall surface. Reverse flow cases where confined water is displaced with the ternary mixture further illustrate the importance of the impact of relative wettability of coexisting phases on boundary displacement. The findings in this work are readily generalized using phase diagrams to provide insights and guidelines for the design of solution formulations for confined liquid displacement. Such displacement processes are important in geological, chemical, and biological processes in enhanced oil recovery, CO_2 sequestration, catalytic reactions and drug delivery systems.

Chapter 4

How fast do microdroplets generated during liquid-liquid phase separation move in a confined 2D space?[1]

4.1 Speed and direction of model oil-rich microdroplets mediated by local composition gradients

At low octanol mass fraction in solution A from 2 to 20 wt-% (Composition 6 to 11 in Table 2.1), a trail of octanol-rich microdroplets is produced. Microdroplets form and are propelled away from the diffusive boundary between water and solution A. The locations of droplet formation are usually at the tip of a triangular protrusion of solution A into the side of the penetrating water. The reason for localized droplet formation is that the composition gradient of octanol is the sharpest at these locations [99]. Figure 4.1A shows the trajectory of a representative droplet after formation. The droplet displacement increases with time with an exponent of $0.75 < n < 1$. Typically, movement is away from a central line drawn through a protrusion, oblique to the x-axis. There does not appear to be a strong dependence on the displacement

[1] This chapter presents the results and discussion of work submitted as **G. F. Arends**, J. M. Shaw, X. Zhang. How fast do microdroplets generated during liquid-liquid phase separation move in a confined 2D space? Energy & Fuels. (2021).

process of the oil-rich droplets as a function of initial octanol composition at low octanol concentrations, as shown in Figure 4.1B.

Figure 4.1C indicates the principal forces acting on a moving oil-rich droplet. The difference in interfacial tension acting on the droplet by a composition gradient induces a shear force along the surface. The shear force on the droplet is a Marangoni-driven stress (F_M) in the direction from a low to high interfacial tension region. As the droplet moves, it experiences a viscous force in the opposite direction by the surrounding liquid, proportional to the velocity of the Marangoni flow. The viscous force (F_{vis}) is related to the droplet radius, the viscosity and the velocity of the surrounding liquid. In addition, the substrate introduces a drag force (F_D) consisting of different forces associated with the wettability of the oil-rich droplet on the hydrophobic substrate. More specifically, the drag force depends on the interfacial tension between the droplet and the solid substrate, and the contact area of the droplet on the surface. Initially, as the droplets are formed, the Marangoni stress is larger than the two opposing forces by a sharp composition gradient at the point of droplet nucleation, which is how the droplet initially becomes mobile. Shortly after, the forces become balanced, which can be deduced from the linear relationship of the displacement with time Figure 4.1B.

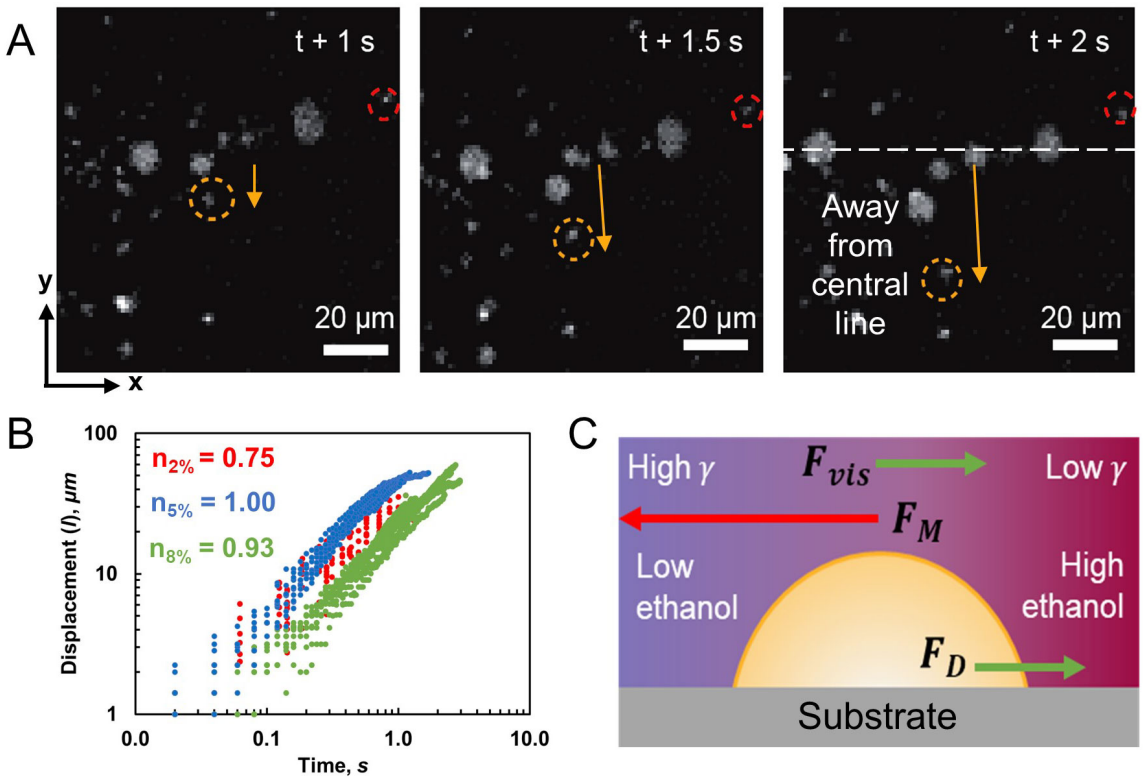

Figure 4.1: (A) Time-based optical images of octanol-rich droplets moving away from a triangular protrusion for solution A with 8 wt-% octanol. The red dotted circle shows a stationary object as a reference. A representative moving droplet is indicated with a yellow dotted circle. (B) Octanol-rich droplet displacement versus time from a stable triangular protrusion for solution A with 2 wt-% (red), 5 wt-% (blue) and 8 wt-% (green) octanol. (C) Sketch of the cross-sectional view of a moving oil-rich droplet with key forces annotated.

We expected the shape of the protrusion to impact the direction and speed of the microdroplets and illustrate this effect using the ternary mixture of butylparaben, ethanol and water. The fluorescence images in Figure 4.2 clearly show a protrusion arising in solution A with 10 wt-% butylparaben in ethanol and the trails of stationary and mobile butylparaben-rich droplets immediately after their formation. The local ethanol mass fraction profile was obtained from the fluorescence intensities along to the protrusion and is shown in Figure 4.2B. The fluorescence intensity is high at the point of butylparaben-rich droplet formation and decreases in the negative x-direction towards the water side. The ethanol composition gradient is sharpest in the

butylparaben-rich continuous phase near the point of formation.

Figure 4.2C and D show two distinct patterns of droplet movement from the phase separation zone. The first pattern is semi-circular with an opening angle of $\omega = 14°$. The second pattern shown in Figure 4.2D possesses an arrow shape with an angle of $\omega = 27°$. Figure 4.2F shows the difference in composition gradients for these two droplet movement patterns. The parameter a at fixed t and x, defined in Equation (2.5), has lower values for steeper x-direction composition gradients. Droplet movement in semi-circular patterns experiences sharper composition gradients along the entire triangular zone compared to the arrow pattern.

Figure 4.2G shows the relation between maximum droplet speed and the angle from the x-axis. While the data are scattered, maximum droplet speed decreases as the angle increases. Droplets moving at higher angles encounter smaller composition gradients and hence less interfacial stress, which reduces the maximum speeds that the droplets can achieve compared to droplets moving at smaller angles.

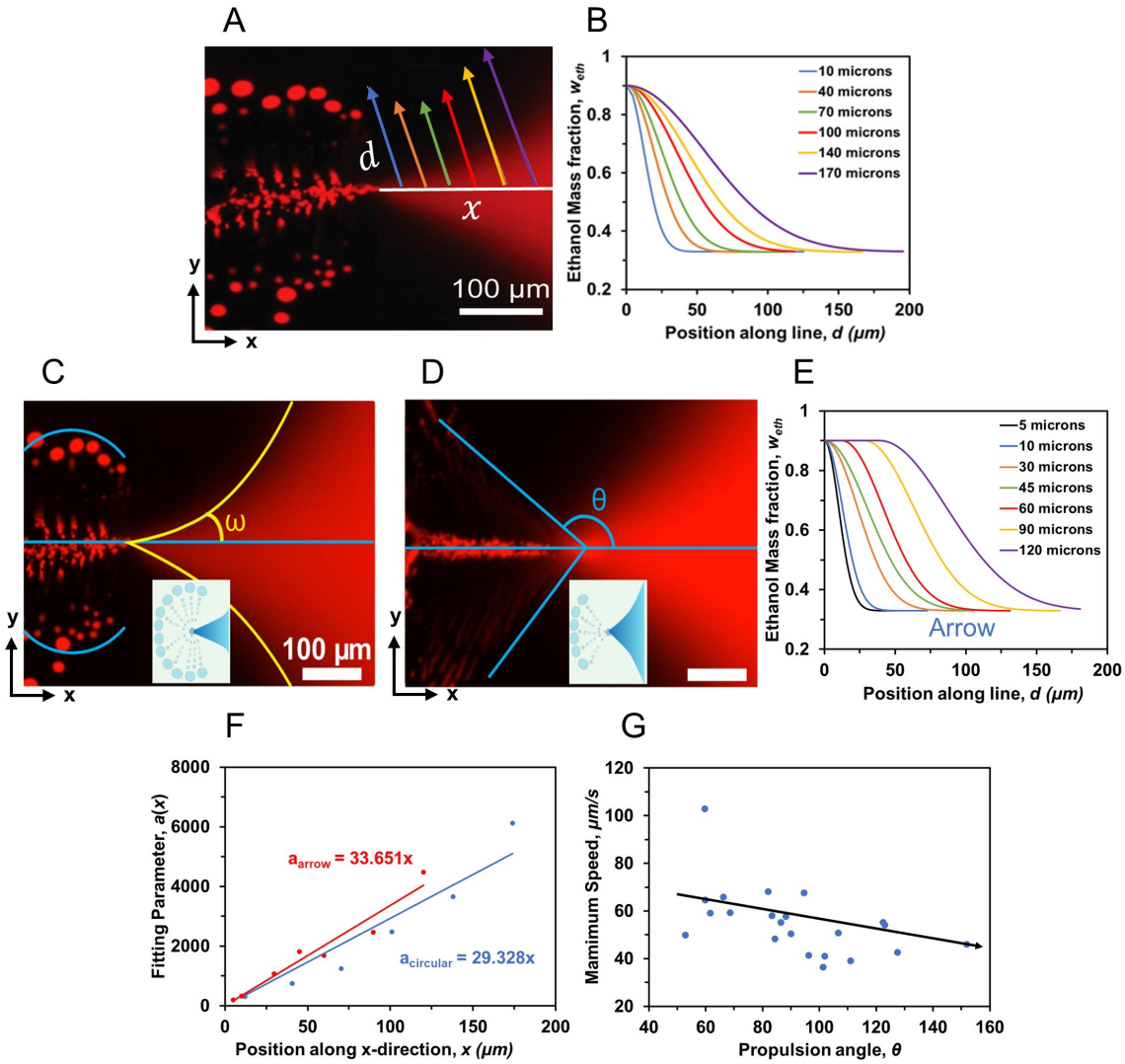

Figure 4.2: Effect of composition gradients on oil-rich droplet movement pattern for solution A with 10 wt-% butylparaben. (A) Fluorescence image of a typical triangular protrusion annotated with data acquisition lines for (B). (B) Ethanol fraction as a function of position along the lines shown in (A). Fluorescence image of (C) semi-circular ($\omega = 14°$) and (D) arrow-shaped ($\omega = 27°$) droplet movement patterns. θ and ω are defined as the angle with the x-axis. (E) Ethanol fraction as a function of position along an arrow-shaped triangular zone. (F) Parameter a, defined in Equation (2.5) values as a function of x-position for semi-circular and arrow shapes. (G) Maximum droplet speed as a function of propulsion angle of droplets θ from phase separation zone.

4.2 Composition of microdroplets in spatially segregated zones arising from liquid-liquid phase separation

Mixing of water with solution A containing octanol from 30 to 35 wt-% produces both oil-rich and water-rich microdroplets, in addition to three spatially separated zones. If we focus on the behaviour for 30 wt-% octanol in solution A (composition 4 in Table 2.1 and annotated in the phase diagram in Figure 2.1A), three well-defined zones are evident in the images (Figure 4.3B). The lipophilic dye indicates the spatial distribution of oil-rich phase domains. A continuous octanol-rich subphase is labelled as zone 3 (close to the side channel) that extends along the positive x-direction. A continuous water-rich subphase is labelled as zone 2 (further from the side channel) that separates zone 1 and 3. Solution A is labelled as zone 1 (furthest from the side channel) that recedes along the positive x-direction. From the phase diagram, tie lines between the water-rich and octanol-rich subphases intersect with ouzo and reverse ouzo regions. Zone 2 and 3 form from primary liquid-liquid phase separation by diffusive mixing of water with solution A. The water-rich microdroplets form in zone 3 after the primary phase separation already creates spatially segregated zones.

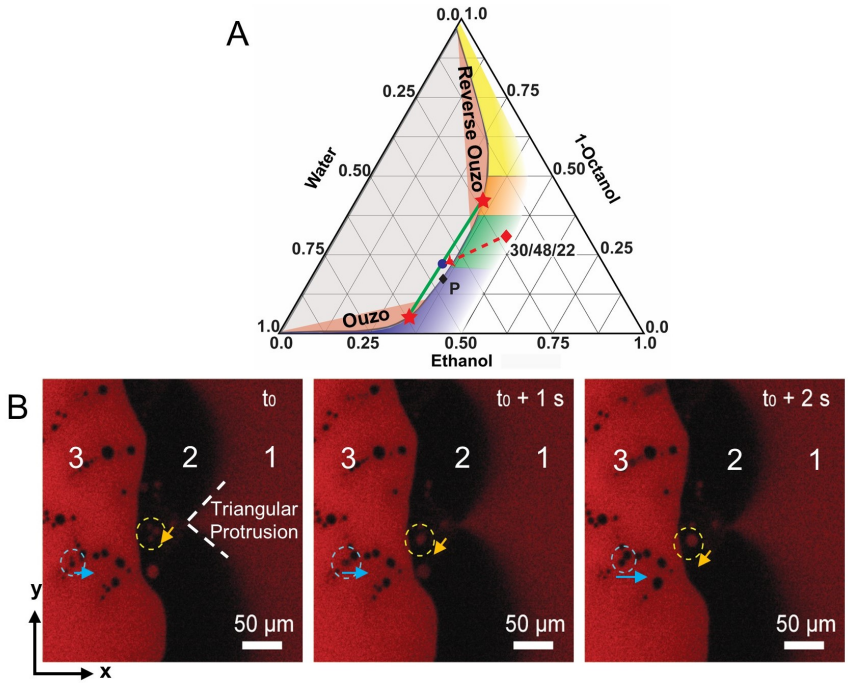

Figure 4.3: (A) Ternary phase diagram indicating the composition of solution A and of the subphases formed from phase separation. Compositions are in mass fractions. Red diamond: solution A; Blue circle: unstable mixture; Black diamond: plait point; Stars: subphases; Green line: tie line; Red dotted line: composition path before phase separation; Pink areas: ouzo region (octanol droplets in water-rich subphase) and reverse ouzo region (water droplets in octanol-rich subphase). Adapted from *Energy Fuels* **2021**, 35, 6, 5194–5205 [23]. (B) A time sequence showing magnified fluorescence images of the three zones developed from phase separation. Zone 1: solution A; Zone 2: water-rich subphase with octanol-rich microdroplets (indicated by orange dashed circle); Zone 3: octanol-rich phase with water-rich droplets (indicated by a blue dashed circle). The orange and blue arrows show directions of droplet movement.

4.3 The motion of oil-rich microdroplets in a water-rich zone

Figure 4.4A shows the movement of one representative octanol-rich microdroplet in zone 2. These droplets are typically 3 μm to 9 μm in lateral diameter, so the channel is only 3 to 4 times larger than the dimension of the largest microdroplets present. The nucleation of octanol-rich droplets in water-rich zone 2 occurs from triangular-shaped protrusions extending from zone 1 (solution A). At the time t (Figure 4.4A), an

octanol-rich droplet detached from the triangular protrusion at the boundary between zone 1 and 2 and propelled in the negative x-direction until it merged with the octanol-rich subphase at the boundary of zone 2 and 3 after 1 s.

Figure 4.4B shows the displacement of ten individual octanol-rich droplets in zone 2 as a function of time, which scales linearly with time ($l \sim t^{0.95}$). The octanol-rich droplets have a broad initial displacement rate which converges to an average displacement rate of (41.9 $\pm$ 4.3) $\mu m/s$ near the zone 2 to zone 3 boundary (Figure 4.4C). The initial and average speeds of octanol-rich droplets in zone 2 are notably slower than for water-rich droplets in zone 3, as will be shown in Figure 4.8.

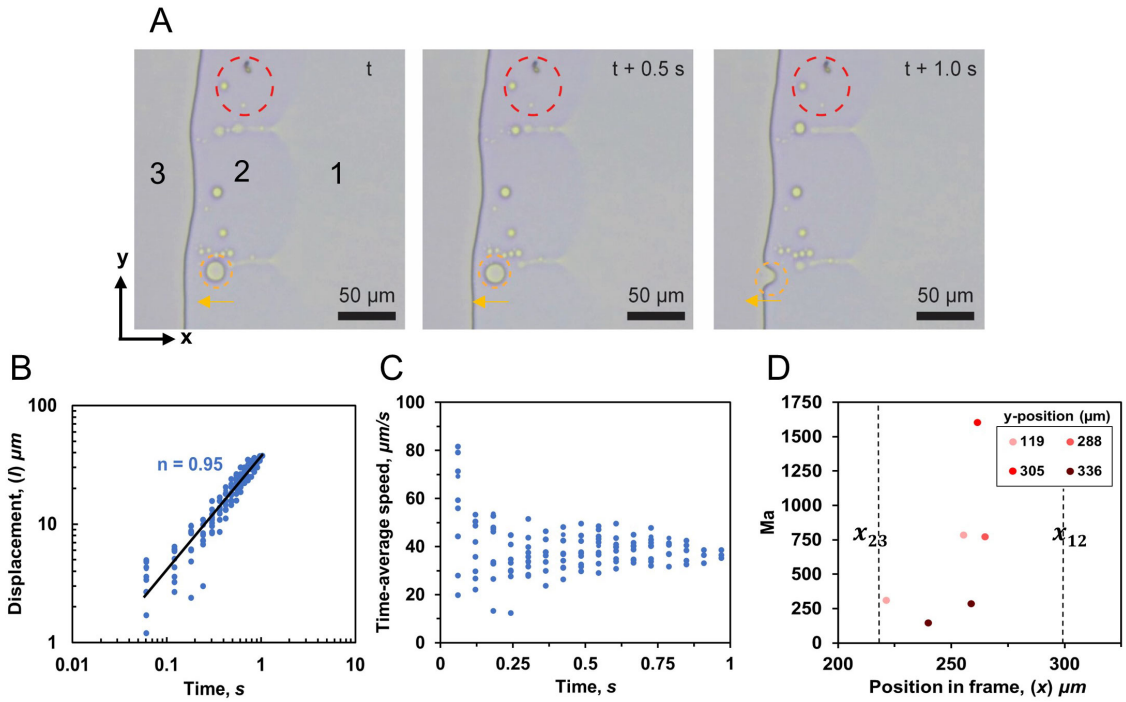

Figure 4.4: Oil-rich droplet displacement for solution A with 30 wt-% octanol. (A) Time-lapsed optical images of octanol-rich droplets formed from triangular protrusions along the zone 2 boundary. The red dashed circle indicates a reference object, and the yellow dashed circle shows a representative octanol-rich droplet. The three zones visible in the field of view are labelled. (B) Displacement of octanol-rich droplets with time after release. (C) Time-averaged octanol-rich droplet speed as a function of time. (D) Marangoni number of octanol-rich droplets as a function of x-direction position at four y-direction positions and at fixed t_0. Triangular protrusions are located at y = 106 μm and y = 312 μm. (x_{12} and x_{23}) indicate the boundary between zone 1 and 2 and the boundary between zone 2 and 3.

Figure 4.5A and C show intensity profiles at two y-values once they have been normalized with respect to the intensity signal from dye-free water at the channel entrance ($x = 0$). Although the plots include image-related noise, the general trend is clear. The fluorescence intensity is almost constant in zone 1. It drops sharply to a valley in zone 2 and increases gradually in zone 3.

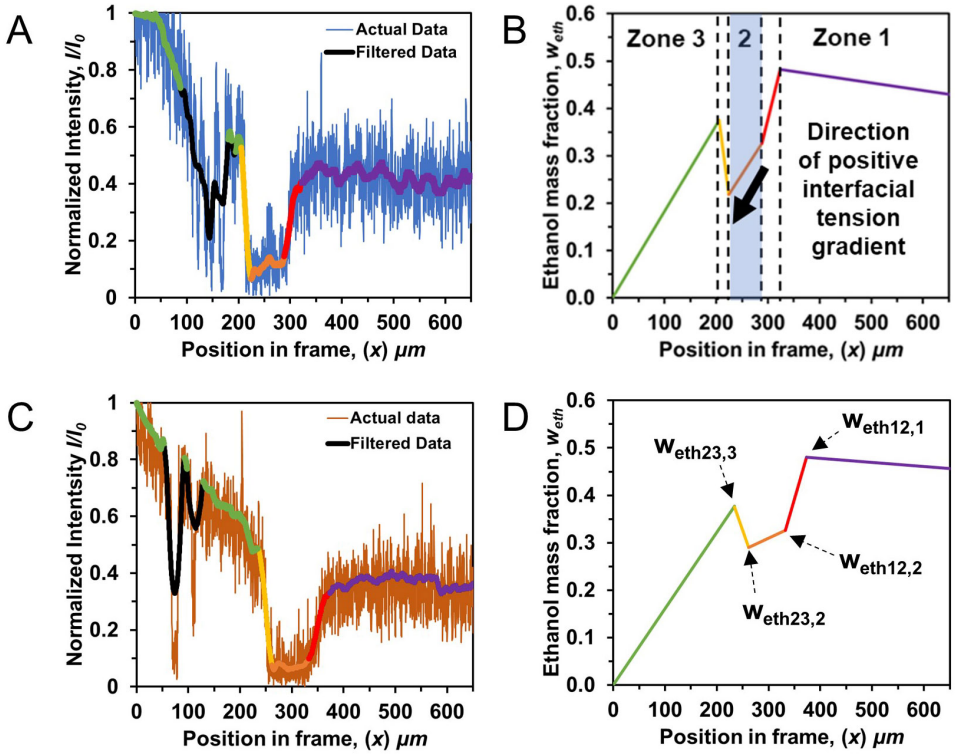

Figure 4.5: Concentration gradients as indicated by fluorescence intensity at t_0 for 30 wt-% octanol in solution A. (A) and (C) Normalized intensity profile as a function of x-position. (B) and (D) Ethanol mass fraction as a function of x-position calculated from intensity profiles. Different colours represent the slope along each zone and boundary.

Spatial gradients in ethanol mass fraction within zone 2 are evaluated from fluorescence intensity (Figure 4.5A). The ethanol mass fraction gradient in zone 2 is (1.99 $\pm$ 1.26) $\times 10^{-3}$ μm^{-1} in the positive x-direction. The ethanol mass fraction gradient jumps to $(4.02 \pm 1.19) \times 10^{-3}$ μm^{-1} in the positive x-direction at the boundary between zone 1 and zone 2. The change in gradient at this boundary is the sharpest at or near a triangular protrusion location and becomes smaller at locations remote

from triangular protrusion. The center of such protrusions is the location where phase separation occurs, causing the sharp concentration gradient.

The gradient of the ethanol mass fraction in zone 2 has important implications for oil-rich microdroplet motion. The interfacial tension between an oil-rich microdroplet and the water-rich continuous phase decreases with increasing ethanol mass fraction. The interfacial tension gradient along a droplet surface in the negative x-direction induces Marangoni stress so that the oil-rich microdroplets move to the direction with higher interfacial tension, consistent with what has recently been reported [99].

The composition gradient applicable to octanol-rich droplets can also be demonstrated with the dimensionless Marangoni number. In this experiment (experiment 4), the composition gradient across an octanol-rich droplet was obtained from ethanol mass fraction as a function of position in zone 2. The Marangoni number values range from $150 < Ma < 1600$ with x-direction (Figure 4.4D) and do not appear to be a function of the y-position value. Here $x = 0$ is defined at the position of the side channel. The Marangoni values are higher than the case of a sub-millimetre oil drop immersed in a stratified ethanol/water liquid ($Ma < 10^3$)[100] but lower than a water/glycerol evaporating drop ($Ma < 10^5$) [101], where both thermal and composition gradients enhance Marangoni flows. In our experiments, while the droplets are very small, the differences in surface tension are significant enough to produce large values Ma number due to the confinement. When liquid-liquid phase separation occurs, the subphases formed have very different compositions which are not able to mix efficiently, resulting in the formation of sharp composition gradients within a confined local space. The surface tension differences $\Delta\sigma$ were obtained as a function of position in the x-direction, which considers the small length scale of the droplets.

The effect of the triangular protrusion on droplet displacement is also observed here, similar to Figure 4.2. Droplets closer to the triangular protrusion in both x and y have higher Marangoni numbers related to sharper composition gradients near the protrusions. The effect in the y-direction is evinced by the high Marangoni number of

the droplet at (x = 261, y = 288), which had the smallest distance from a triangular protrusion in the data set.

Two additional ternary systems were examined to further demonstrate the features of propelling oil-rich microdroplets and the evolution of the oil-rich zone. As shown in Figure 4.6, a similar three-zone configuration is formed for solution A comprising HDODA or oleic acid, water and ethanol as compositions labelled in the phase diagrams shown in Figure 2.1. Lines of HDODA-rich droplets are ejected from the undulating boundary between the water-rich zone and solution A. These droplets coalesce rapidly and merge with the HDODA-rich zone on the other side of the water-rich zone. The speed of HDODA-rich microdroplets ranges from 20 to 80 $\mu m/s$, slower than octanol-rich microdroplets in general. The process reveals that the oil-rich zone develops from merged propelling microdroplets. Meanwhile, the water-rich droplets within the HDODA-rich zone nucleate and grow on the surface, remaining immobilized throughout the entire process.

By contrast, no water-rich microdroplets are formed in the oil-rich zone for the oleic acid, ethanol and water ternary. The boundary between the water-rich zone and the oleic acid solution is rough and evolves rapidly with time. The water-rich subphase forms an elongated zone. Microdroplets of oleic acid form and pinch off along the entire boundary instead of at the tips of protrusions. The speed of oleic acid-rich microdroplets can reach 150 $\mu m/s$, faster than that of HDODA-rich and octanol-rich microdroplets. In addition, the droplets travel for a longer distance without coalescing with nearby droplets. The results for the diverse mixtures demonstrate that the propelling droplet behaviour and development of segregated zones are general phenomena for liquid-liquid phase separation in confined spaces, although the speed of droplets and zone boundary shape may vary among ternary solutions.

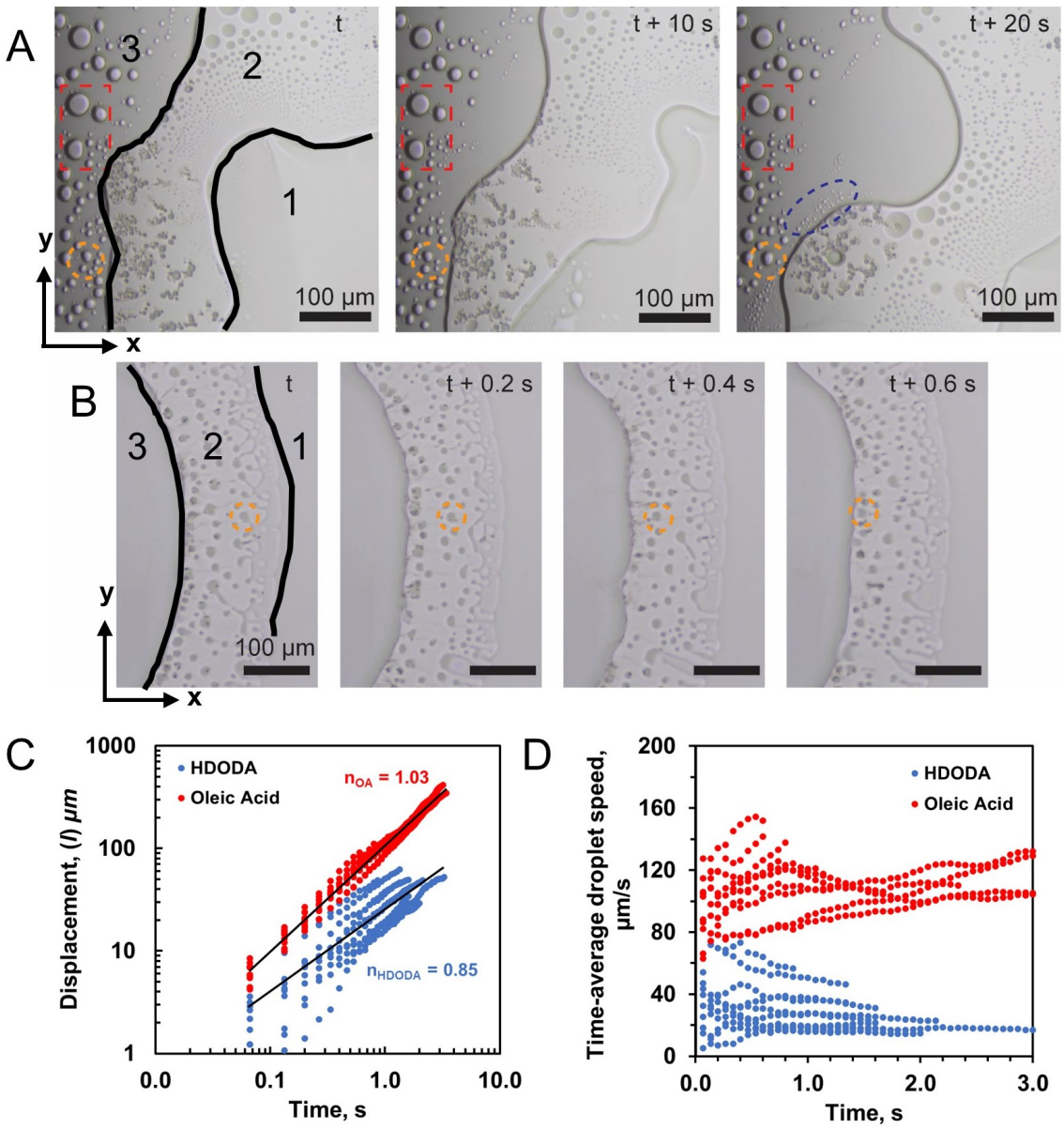

Figure 4.6: Time-based optical images of three-zone configurations for model oils HDODA and Oleic acid in solution A. (A) 25 wt-% HDODA/50 wt-% ethanol/25 wt-% water in solution A. The red dashed box indicates reference stationary water-rich droplets within the oil-rich zone. The yellow dashed circle indicates a representative water-rich droplet that coalesces with nearby growing droplets. The blue dashed circle indicates the spontaneous growth of small water-rich droplets close to the moving boundary. (B) 24 wt-% Oleic Acid/49 wt-% ethanol/27 wt-% water as solution A. The yellow dashed circle indicates the movement of one representative oleic acid-rich droplet towards the oil-rich zone with time. (C) Displacement of oil-rich droplets with time for HDODA (blue) and oleic acid (red) as model oils. Linear fit applied to show scaling. (D) Time-averaged oil-rich droplet speed as a function of time.

4.4 The motion of water-rich microdroplets in an oil-rich zone

At low oil concentration in solution A, the fast motion of propelling oil-rich microdroplets induces a directional flow in the narrow chamber to replenish the liquid loss at the location of phase separation due to mass conservation. Such directional transport induced by propelling oil-rich microdroplets is also expected to be present at high oil concentrations with separated zones. Without tracer nanodroplets at high oil concentration, the presence of the induced flow can actually be inferred from the motion of water-rich microdroplets.

Behind the protrusion in zone 2, water-rich microdroplets form on the surface in zone 3. These droplets give rise to low fluorescence intensity signals within a high fluorescence intensity phase, suggesting the droplets consist mainly of a water-rich solution (Figure 4.7A). Unlike oil-rich microdroplets, water-rich droplets do not propel immediately after their formation. Near the oil-rich zone 3 boundary, some water-rich microdroplets detach from the surface and move suddenly in the positive x-direction. After a short time, these moving water-rich microdroplets merge with zone 2. The displacements (l) of representative water-rich droplets show a clear linear relationship with time (t), as illustrated in Figure 4.7B. The linearity of their motion indicates that this droplet movement cannot be attributed to Brownian motion where l is expected to scale with $t^{1/2}$.

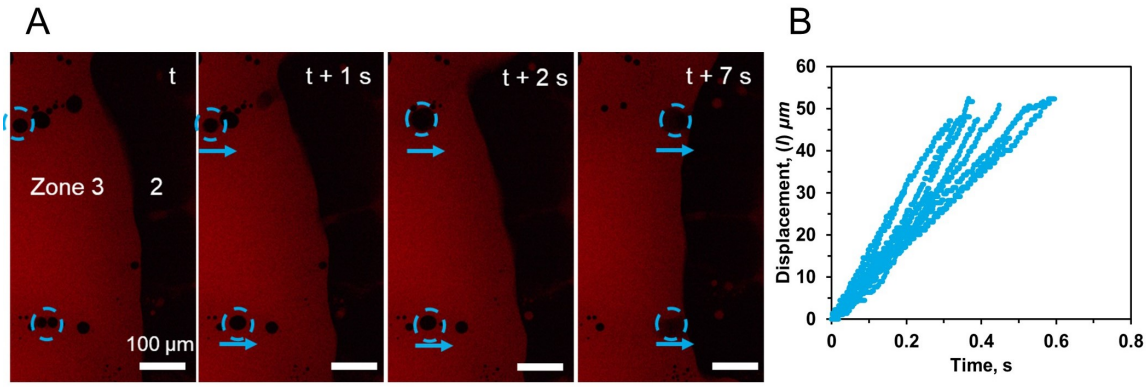

Figure 4.7: (A) Time-based fluorescence image of water-rich droplet movement at the 30 wt-% octanol composition. Dashed circles indicate the movement of two water-rich droplets within zone 3. (B) Displacement of water-rich droplets in zone 3 as a function of time. Each set of dots represents the motion of one droplet measured with a high-speed camera. The final displacement position of each droplet is when they merge with the boundary between zone 2 and 3.

The motion of those water-rich microdroplets is not due to Marangoni stress in zone 3. The fluorescence intensity decreases in the x-direction in zone 3, as shown in Figure 4.5, suggesting that the ethanol mass fraction in the continuous phase increases as the boundary between zone 3 and 2 is approached. The highest ethanol mass fraction is located at the boundary where the ethanol mass fraction in zone 3 has not been influenced by water diffusion as the oil-rich subphase is newly formed from the phase separation. The ethanol mass fraction in the oil-rich continuous phase is estimated from the fluorescence intensity, as outlined in the Experimental Section. A spatial gradient of $(1.72 \pm 0.07) \times 10^{-3}\ \mu m^{-1}$ is obtained from six y-position values in zone 3.

In zone 3, the majority of water-rich microdroplets far from the boundary of the two zones remain stationary. The stability of these water-rich microdroplets suggests that the high viscosity of the oil-rich continuous phase may hinder the movement of water-rich microdroplets, even in the presence of a large composition gradient. For those moving water-rich droplets, their motion is toward lower surface tension (i.e. higher ethanol fraction). The gradient in the ethanol fraction is expected to pull water-rich

microdroplets in the negative x-direction opposite to what is observed. Instead of the Marangoni effect, the movement of these water-rich droplets is attributed to the directional flow induced by propelling oil-rich microdroplets in the water-rich zone. In other words, the motion of water-rich microdroplets in zone 3 originates from the composition gradient in zone 2 through induced flow.

The induced flow was visible in our previous work where nanodroplets as the tracers were suspended in the liquid phase [99]. The flow velocity was measured to be 45 μ/s near a protrusion. Here we could not detect the induced flow in experiments as no nanodroplets formed in the surrounding to reveal the flow. However, the principle of mass conservation still holds in our confinement, the induced flow is expected to maintain mass loss in zone 2.

Figure 4.8A shows the time-averaged speed of nine water-rich droplets in zone 3 over a displacement window of (47.2 ± 10.3) μm. Their trajectories are characterized by high initial speeds that decay within a few microns to a minimum of (58 ±20) $\mu m/s$. Droplet speeds then gradually increase to an average speed of (119 ± 24) $\mu m/s$. Droplets merge with the boundary at d_{final} (total distance travelled by the droplet to reach the boundary between zones 2 and 3 at x_{23}). As the driving force from induced flow and the drag effect from the hydrophobic bottom surface and the surrounding octanol-rich subphase may reach transient balance, the speed of the water-rich droplets remains relatively constant until they reach the boundary between zones 2 and 3.

The Reynolds number, Re, of the water-rich droplets are of the order 10^{-4} calculated with

$$Re = \frac{UR}{\nu} \tag{4.1}$$

where R is the droplet radius, ν the kinematic viscosity of the surrounding liquid in zone 3, and U is the relative droplet speed [51]. For such low Reynolds numbers, viscous dissipation dominates.

The viscosity of the oil-rich continuous phase in zone 3 is high, which may lead to

faster decay in the speed of water-rich microdroplets after the initial rapid motion, as shown in the insert of Figure 4.8A. As the bottom surface is hydrophobic, this implies that the water-rich microdroplets experience a strong drag force as they displace oil-rich subphase from the surface. The shear arising from the directional flow is sufficiently strong to overcome both viscous dissipation from the oil-rich continuous phase and the drag force from the hydrophobic surface.

Figure 4.8B provides the average speed of water-rich droplets with diameters from 3 to 6.5 μm. For a given droplet diameter, the speed scatters in a large range. However, the overall trend is toward lower speeds for larger droplets. Water-rich droplets furthest from the zone 3 boundary shown in Figure 4.5C, near ($x = 0$), are typically larger in size due to coalescence with nearby droplets. Some of the large water-rich droplets remain immobilized on the hydrophobic bottom surface, suggesting that the experienced drag forces must be overcome to trigger droplet motion. Microdroplets closer to the zone 3 boundary are smaller in size and are more mobile due to a reduced surface area.

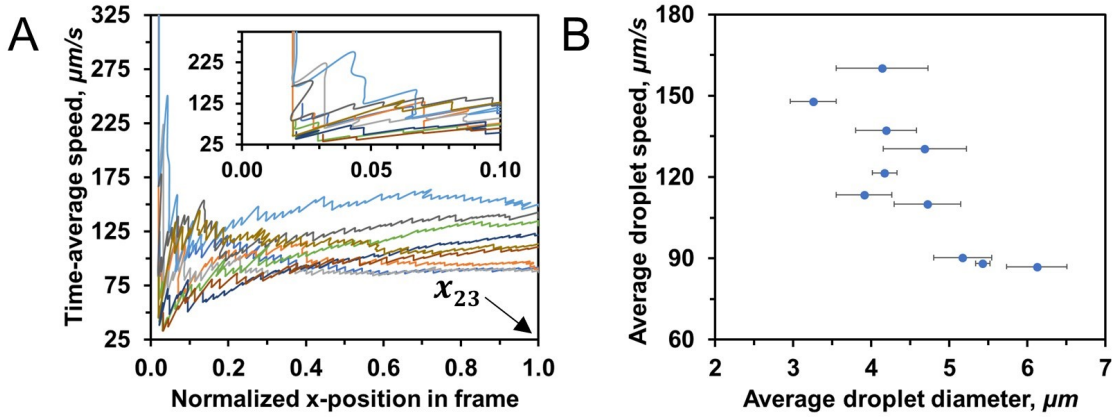

Figure 4.8: (A) Time-averaged droplet speed as a function of normalized droplet displacement. Inset: zoom-in plot of early displacement. (B) Water-rich droplet speed as a function of average droplet size at 30 wt-% octanol composition.

For solution A with 35 wt-% octanol, phase separation and the droplet motion are qualitatively similar to what was described above at 30 wt-% octanol. Figure 4.9A

shows bright-field images of water-rich droplets for this case. Water-rich droplets in zone 3, far from the boundary with zone 2, form branch-like patterns observed previously for the diffusion-dominated ouzo effect in confinement [43].

Figure 4.9B compares the displacement of water-rich droplets with time for 30 and 35 wt-% octanol in solution A. Water-rich droplets from solution A with 35 wt-% octanol are displaced for a shorter distance and at a slower displacement rate on average (23 ± 10 μm/s) compared to those from a solution A with 30 wt-% octanol. The water-rich droplets show dynamic behaviour similar to the nanodroplet tracers in the replenishing flow [99]. The resulting transport mechanism differs significantly from diffusion-based transport, which scales with $l \sim t^{1/2}$ in 2D confinement [43].

Figure 4.9C shows the normalized diameter of water-rich mobile droplets as a function of normalized x-position, where the normalization was performed by dividing local droplet diameter by the initial droplet diameter, and x-position was normalized by subtracting the initial position value from the position value and then dividing by the distance from the initial position to the boundary between zone 2 and 3 (x_{23}). The mean droplet size increases as the boundary between zone 2 and 3 is approached, suggesting the water-rich phase increases within the droplet by diffusion as the droplets approach water-rich zone 2.

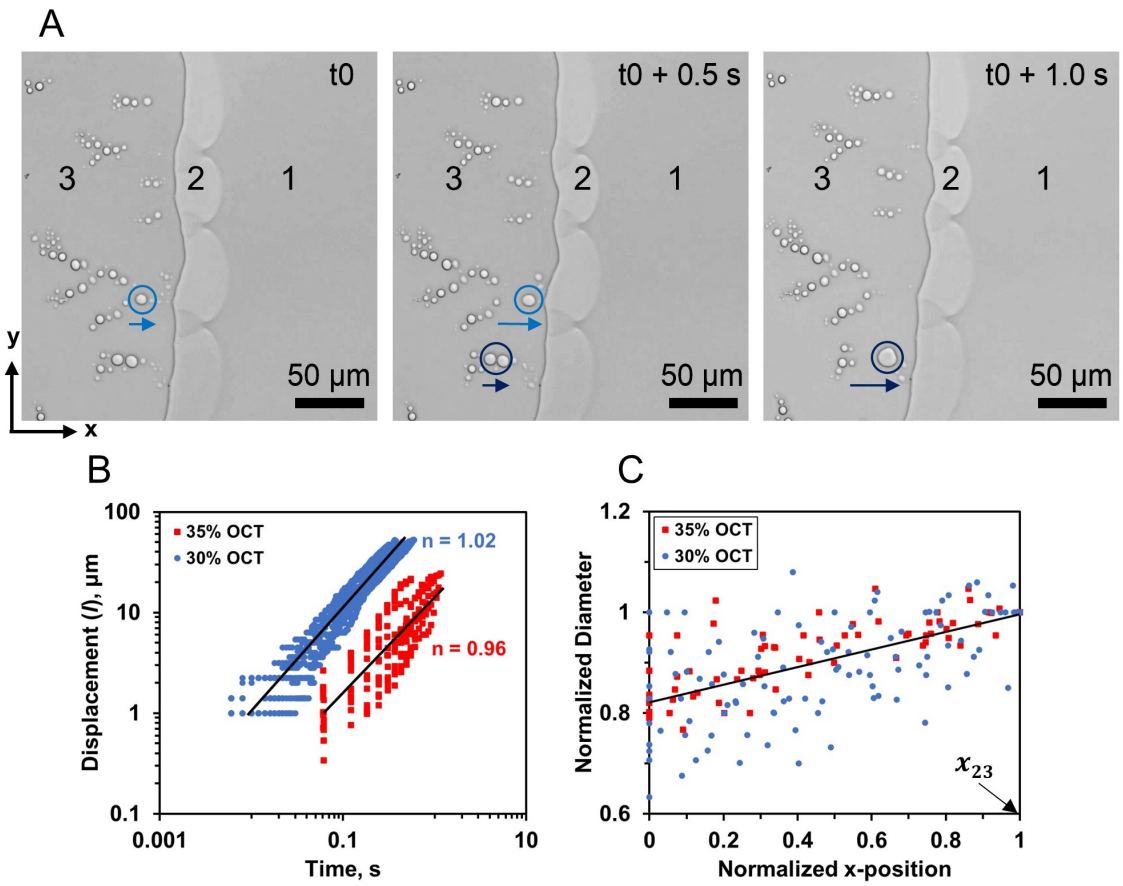

Figure 4.9: Comparison between initial solution compositions. (A) Time-based optical images of water-rich droplet movement in zone 3 with 35 wt-% octanol in solution A. (B) Displacement of water-rich droplets in zone 3 as a function of time with 30 wt-% and 35 wt-% octanol in solution A. (C) Normalized water-rich droplet diameter as a function of normalized x-position in zone 3.

The motion of the microdroplets can be enhanced by coalescence, as shown in Figure 4.10. The images show a section of the oil-rich zone that initially did not contain water-rich droplets. With time, droplet nucleation and subsequent growth occurred from t to $t + 8s$. At $t + 10s$, two droplets coalesce, driving the motion of the now larger droplet toward the boundary with the water-rich zone. The phenomenon of a jumping drop induced by coalescence of two parent drops has been investigated extensively [102–106]. The reduction in the interfacial energy from coalescence contributes to the kinetic energy of the jumping drop. It is notable that in the confined space, droplet coalescence can also enhance the motion of the merged drop.

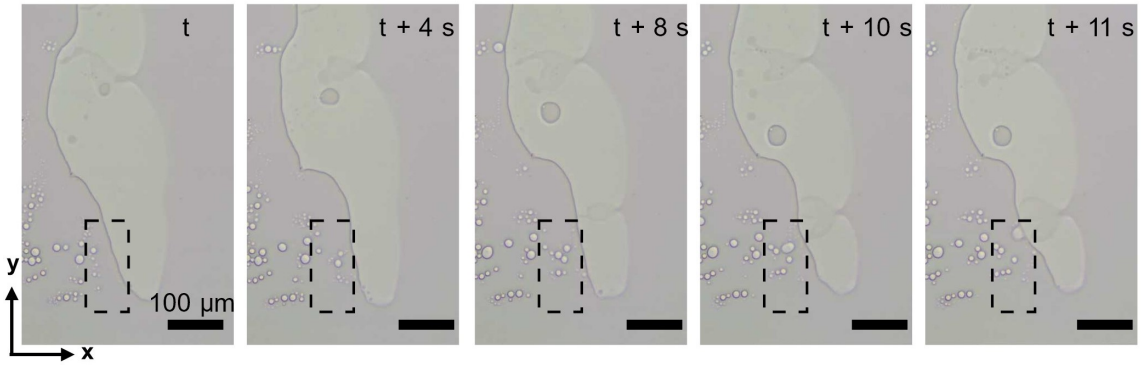

Figure 4.10: Time-based optical images at the 35 wt-% octanol solution composition showing water-rich droplet nucleation, growth and subsequent coalescence.

4.5 A comparison of the speed of octanol-rich and water-rich microdroplets

The exponent values obtained from the displacement versus time at octanol compositions in solution A from 2 to 30% (Compositions 4-11 in Table 2.1), presented in Figure 4.11A, were found to scale ($l \sim t^{0.96}$) with an expected uncertainty of $\pm$ 0.10. However, at 2 wt-% octanol, the displacement of octanol-rich droplets scaled with ($l \sim t^{0.75}$). At 10 wt-% octanol composition, the protrusion shape changes from a triangular shape to a line shape where the displacement of droplets scaled with an n value approaching the displacement behaviour of evaporating droplets spreading on a liquid substrate ($l \sim t^{1.2}$) [107]. These scaling results indicate the balance between the Marangoni stress and viscous stress on droplet movement, as was observed for droplet movement enhanced by the Marangoni stress produced from concentration gradients [108].

Figure 4.11B shows the average droplet speed at all positions as a function of octanol composition in solution A from 2 to 35 wt-%. We have included octanol-rich droplet speeds arising from different boundary shape features, in addition to data on water-rich droplets in the oil-rich zone. The results indicate an overall increasing trend of oil-rich droplet speed from 2 to 20 wt-% octanol composition, which then decreases

at the 30 wt-% compositions. A maximum value of oil-rich droplet speed is suspected from a composition that intersects the phase boundary close to the plait point, as the trend suggests. At 10 to 20 wt-% octanol compositions, octanol-rich droplets formed from triangular protrusions and line-shaped protrusions at the boundary location. The results summarized show that droplets from the triangular-shaped protrusions displace faster than those from the line-shaped protrusions. The composition gradient along a line-shaped protrusion is expected to be less steep compared to one from a triangular protrusion. If we consider our previous results (Figure 4.2G), the larger the angle of the protrusion ω, the larger the propulsion angle θ, and thus the slower the droplet speeds.

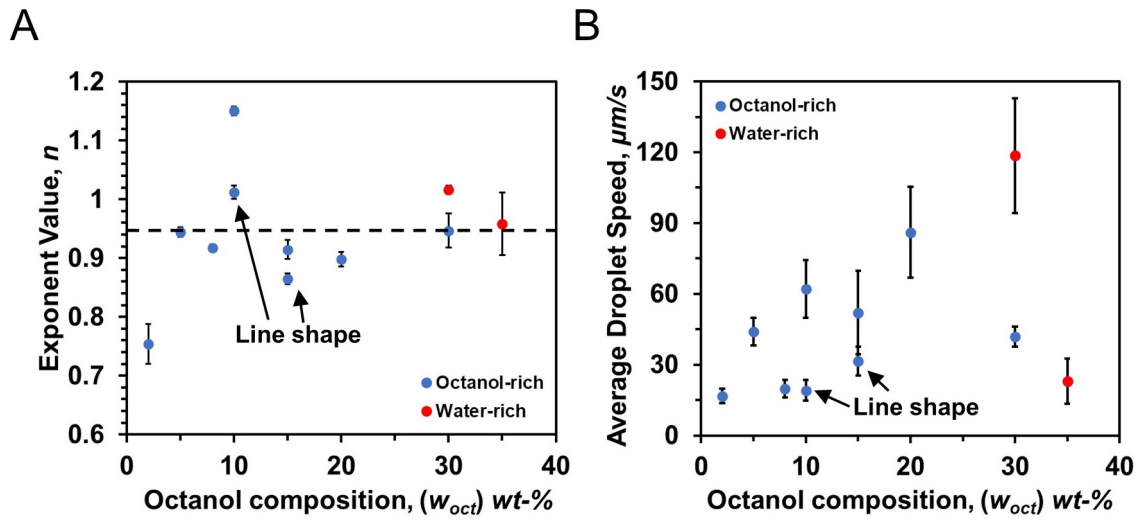

Figure 4.11: (A) Droplet displacement scaling as a function of octanol wt-% in solution A. (B) Average droplet speed as a function of octanol wt-% in solution A. Oil-rich droplets formed from line-shaped protrusions are annotated.

4.6 Conclusion

We show that oil-rich microdroplets confined in a 2D chamber can travel at speeds up to 150 $\mu m/s$. The motion of oil-rich microdroplets in the water-rich zone is driven by local composition gradients arising from liquid-liquid phase separation during diffusive mixing of water as a poor solvent with a ternary liquid mixture. The fast motion of oil-rich microdroplets induces directional flow in the confined space, mobilizing water-rich microdroplets in the oil-rich zone. For both water-rich microdroplets in an oil-rich zone and oil-rich droplets in a water-rich zone formed during phase separation, the displacement of the microdroplets scales linearly with time. We show the sharpest composition gradient is created at the locations where the droplets form. The speed of droplets is responsive to the shape of the local diffusive mixing boundary. Our findings highlight the possibility of enhanced transport phenomenon via liquid-liquid phase separation in confined spaces.

Chapter 5

Conclusions, & future work

5.1 Main results & contributions

The work in this thesis showed the potential of using liquid-liquid phase separation to enhance liquid transport within confinement. The displacement process of the boundary between a confined liquid and a penetrating liquid was followed in-situ within a confined solvent exchange microfluidics chamber. The boundary between the two solutions was affected by the initial solution composition of the confined liquid, which resulted in four displacement regimes, each with their own liquid-liquid phase separation mechanisms. The boundary changes from an insoluble to a diffusive boundary with the decrease in initial oil composition. Regimes consisting of the higher oil compositions are preferred for displacing liquids, while those at lower compositions are best for separation and extraction of the model oil from the solution at lower displacement rates. Regardless of the initial composition, there were enhancements to the liquid transport far exceeding that expected of a single-phase diffusive displacement process. Further improvements to the displacement were observed by adding some amount of the good solvent to the displacing liquid improving its wettability on the wall surface. At the microscopic level, liquid transport was also enhanced by the movement of oil-rich and water-rich droplets formed during the phase separation. The oil-rich droplets responded to sharp local chemical composition gradients producing droplet speeds up to 150 $\mu m/s$ and water-rich droplets became mobile by

an induced flow. The findings of this thesis work provide a better understanding of the possibilities of using liquid-liquid phase separation as a method to improve liquid transport within confined spaces.

5.2 Recommendations for future work

This thesis work explored the displacement behaviour of the liquid-liquid phase separating ternary mixtures by concentrating on the effects at different initial solution compositions. There are several other technical and practical issues that deserve further investigation in future research.

1. The effect of changing the ternary system to complete the organic phase. While we showed the effects of liquid-liquid phase separation for several model oils in this thesis, all the ternary systems were aqueous-based.

2. The effects of level of confinement. The channel height for all of these experiments was within the same range of 20 to 30 microns. It would be beneficial to know at what length scales the enhancing effects of transport start to diminish. We could use fabricated microchambers with more precise control of the channel height. Additionally, it would be interesting to determine the effects of both vertical and lateral confined areas by reducing the width dimension of the channel.

3. The improvement of detection techniques for the chemical mapping of the exact composition in time and space is required. The method used in this thesis required several assumptions and steps to roughly approximate a composition gradient. A technique such as Raman confocal microscopy may be used to determine the spatiotemporal evolution of the chemical species.

4. The effect of surface roughness by using patterned microstructures instead of chemically modified smooth surfaces. We previously explored the effects of

surface wettability on droplet displacement, and we know that droplet displacement is enhanced in some conditions. However, we have not yet explored the effects of using patterned substrates, which could enhance the transport even further.

Bibliography

[1] A. Perazzo, G. Tomaiuolo, V. Preziosi, and S. Guido, "Emulsions in porous media: From single droplet behavior to applications for oil recovery," *Adv. Colloid Interface Sci.*, vol. 256, pp. 305–325, 2018.

[2] V. Guillen, M. Carvalho, and V. Alvarado, "Pore scale and macroscopic displacement mechanisms in emulsion flooding.," *Transp. Porous Media*, vol. 94, pp. 197–206, 2012.

[3] Y. Zhang, W. Yu, K. Sepehrnoori, and Y. Di, "Investigation of nanopore confinement on fluid flow in tight reservoirs.," *J. Pet. Sci. Eng.*, vol. 150, pp. 265–271, 2017.

[4] P. Druetta and F. Picchioni, "Surfactant flooding: The influence of the physical properties on the recovery efficiency.," *Petroleum*, vol. 6, pp. 149–162, 2020.

[5] B. Grambow, "Mobile fission and activation products in nuclear waste disposal," *J. Contam. Hydrol.*, vol. 102, no. 3-4, pp. 180–186, 2008.

[6] Z. Ziabakhsh-Ganji, H. M. Nick, M. E. Donselaar, and D. F. Bruhn, "Synergy potential for oil and geothermal energy exploitation," *Appl. Energy*, vol. 212, pp. 1433–1447, 2018.

[7] B. Li and S. M. Benson, "Influence of small-scale heterogeneity on upward co2 plume migration in storage aquifers," *Advances in Water Resources*, vol. 83, pp. 389–404, 2015.

[8] J. Gao, H. Xing, Z. Tian, J. Pearce, M. Sedek, S. Golding, and V. Rudolph, "Reactive transport in porous media for co2 sequestration: Pore scale modeling using the lattice boltzmann method.," *Comput. Geosci.*, vol. 98, pp. 9–20, 2017.

[9] D. Feng, K. Wu, X. Wang, J. Li, and X. Li, "Modeling the confined fluid flow in micro-nanoporous media under geological temperature and pressure.," *Int. J. Heat Mass Transf.*, vol. 145, p. 118 758, 2019.

[10] P. Kortunov, S. Vasenkov, J. Kärger, M. Fé Elía, M. Perez, M. Stöcker, G. Papadopoulos, D. Theodorou, B. Drescher, G. McElhiney, *et al.*, "Diffusion in fluid catalytic cracking catalysts on various displacement scales and its role in catalytic performance," *Chem. Mater.*, vol. 17, no. 9, pp. 2466–2474, 2005.

[11] J. Tao, X. Song, T. Zhao, S. Zhao, and H. Liu, "Confinement effect on water transport in cnt membranes.," *Chem. Eng. Sci.*, vol. 192, pp. 1252–1259, 2018.

[12] T. Pak, L. F. de Lima Luz, T. Tosco, G. S. R. Costa, P. R. R. Rosa, and N. L. Archilha, "Pore-scale investigation of the use of reactive nanoparticles for in situ remediation of contaminated groundwater source," *Proc. Natl. Acad. Sci. U.S.A*, vol. 117, no. 24, pp. 13 366–13 373, 2020.

[13] K. Wu, Z. Chen, J. Li, X. Li, J. Xu, and X. Dong, "Wettability effect on nanoconfined water flow.," *Proc. Natl. Acad. Sci. U.S.A.*, vol. 114, pp. 3358–3363, 2017.

[14] R. Liuzzi, A. Carciati, S. Guido, and S. Caserta, "Transport efficiency in transdermal drug delivery: What is the role of fluid microstructure?" *Colloids Surf. B*, vol. 139, pp. 294–305, 2016.

[15] R. Liuzzi, V. Preziosi, S. Caserta, and S. Guido, "Development of model systems for in vitro investigation of transdermal transport pathways," *Can. J. Chem. Eng.*, vol. 95, no. 9, pp. 1637–1645, 2017.

[16] R. Radhakrishnan, S. Farokhirad, D. M. Eckmann, and P. S. Ayyaswamy, "Nanoparticle transport phenomena in confined flows.," *Adv. Heat Transf.*, vol. 51, pp. 55–129, 2019.

[17] W. Sanhai, J. Sakamoto, R. Canady, and M. Ferrari, "Seven challenges for nanomedicine.," *Nat. Nanotechnol.*, vol. 3, pp. 242–244, 2008.

[18] W. Sparreboom, A. van den Berg, and J. Eijkel, "Principles and applications of nanofluidic transport.," *Nat. Nanotechnol.*, vol. 4, pp. 713–720, 2009.

[19] D. Tartakovsky and M. Dentz, "Diffusion in porous media: Phenomena and mechanisms.," *Transp. Porous Med.*, vol. 130, pp. 105–127, 2019.

[20] S. B. Fredriksen, A. U. Rognmo, and M. A. Fernø, "Pore-scale mechanisms during low salinity waterflooding: Oil mobilization by diffusion and osmosis," *J. Pet. Sci. Eng.*, vol. 163, pp. 650–660, 2018.

[21] R. Aziz, V. Niasar, H. Erfani, and P. J. Martínez-Ferrer, "Impact of pore morphology on two-phase flow dynamics under wettability alteration," *Fuel*, vol. 268, p. 117 315, 2020.

[22] T. Ho and Y. Wang, "Enhancement of oil flow in shale nanopores by manipulating friction and viscosity.," *Phys. Chem. Chem. Phys.*, vol. 21, pp. 12 777–12 786, 2019.

[23] G. F. Arends, J. B. You, J. M. Shaw, and X. Zhang, "Enhanced displacement of phase separating liquid mixtures in 2d confined spaces," *Energy Fuels*, vol. 35, no. 6, pp. 5194–5205, 2021.

[24] C. T. Gerold, A. T. Krummel, and C. S. Henry, "Microfluidic devices containing thin rock sections for oil recovery studies," *Microfluid. Nanofluidics*, vol. 22, no. 7, pp. 1–7, 2018.

[25] V. A. Lifton, "Microfluidics: An enabling screening technology for enhanced oil recovery (eor)," *Lab Chip*, vol. 16, no. 10, pp. 1777–1796, 2016.

[26] M. Saadat, P. A. Tsai, T.-H. Ho, G. Øye, and M. Dudek, "Development of a microfluidic method to study enhanced oil recovery by low salinity water flooding," *ACS Omega*, vol. 5, no. 28, pp. 17 521–17 530, 2020.

[27] L.-X. Zhang, X.-H. Cao, W.-P. Cai, and Y.-Q. Li, "Observations of the effect of confined space on fluorescence and diffusion properties of molecules in single conical nanopore channels," *J. Fluoresc.*, vol. 21, no. 5, pp. 1865–1870, 2011.

[28] W. Xu, J. Ok, F. Xiao, K. Neeves, and X. Yin, "Effect of pore geometry and interfacial tension on water-oil displacement efficiency in oil-wet microfluidic porous media analogs.," *Phys. Fluids*, vol. 26, p. 093 102, 2014.

[29] A. Mandal, A. Samanta, A. Bera, and K. Ojha, "Characterization of oil- water emulsion and its use in enhanced oil recovery," *Ind. Eng. Chem. Res.*, vol. 49, no. 24, pp. 12 756–12 761, 2010.

[30] F. Yu, H. Jiang, Z. Fan, F. Xu, H. Su, and J. Li, "Formation and flow behaviors of in situ emulsions in heavy oil reservoirs," *Energy Fuels*, vol. 33, no. 7, pp. 5961–5970, 2019.

[31] Y. Zhou, D. Yin, W. Chen, B. Liu, and X. Zhang, "A comprehensive review of emulsion and its field application for enhanced oil recovery.," *Energy Sci. Eng.*, vol. 7, pp. 1046–1058, 2019.

[32] S. P. Callender, J. A. Mathews, K. Kobernyk, and S. D. Wettig, "Microemulsion utility in pharmaceuticals: Implications for multi-drug delivery," *Int. J. Pharm.*, vol. 526, no. 1-2, pp. 425–442, 2017.

[33] J. Flanagan and H. Singh, "Microemulsions: A potential delivery system for bioactives in food," *Crit. Rev. Food Sci. Nutr.*, vol. 46, no. 3, pp. 221–237, 2006.

[34] M. Broens and E. Unsal, "Emulsification kinetics during quasi-miscible flow in dead-end pores," *Adv. Water Resour.*, vol. 113, pp. 13–22, 2018.

[35] C. Solans, D. Morales, and M. Homs, "Spontaneous emulsification," *Curr. Opin. Colloid Interface Sci.*, vol. 22, pp. 88–93, 2016.

[36] H.-J. Butt, K. Graf, and M. Kappl, *Physics and chemistry of interfaces*. John Wiley & Sons, 2013.

[37] C. A. Miller, "Spontaneous emulsification produced by diffusion—a review," *Colloids Surf.*, vol. 29, no. 1, pp. 89–102, 1988.

[38] S. A. Vitale and J. L. Katz, "Liquid droplet dispersions formed by homogeneous liquid-liquid nucleation: "The Ouzo effect"," *Langmuir*, vol. 19, no. 10, pp. 4105–4110, 2003.

[39] H. Zhang, X. Ji, P. Li, C. Liu, J. Lou, Z. Wang, W. Wen, Y. Xiao, M. Zhang, and X. Zhu, "Liquid-liquid phase separation in biology: Mechanisms, physiological functions and human diseases," *Sci. China Life Sci.*, vol. 63, no. 7, pp. 953–985, 2020.

[40] S. Alberti, A. Gladfelter, and T. Mittag, "Considerations and challenges in studying liquid-liquid phase separation and biomolecular condensates," *Cell*, vol. 176, no. 3, pp. 419–434, 2019.

[41] T. N. Zemb, M. Klossek, T. Lopian, J. Marcus, S. Schöettl, D. Horinek, S. F. Prevost, D. Touraud, O. Diat, S. Marčelja, and W. Kunz, "How to explain microemulsions formed by solvent mixtures without conventional surfactants," *Proc. Natl. Acad. Sci., USA*, vol. 113, pp. 4260–4265, 2016.

[42] J. Qian, G. F. Arends, and X. Zhang, "Surface nanodroplets: Formation, dissolution, and applications," *Langmuir*, vol. 35, no. 39, pp. 12 583–12 596, 2019.

[43] Z. Lu, M. H. K. Schaarsberg, X. Zhu, L. Y. Yeo, D. Lohse, and X. Zhang, "Universal nanodroplet branches from confining the ouzo effect," *Proc. Natl. Acad. Sci., USA*, vol. 114, pp. 10 332–10 337, 2017.

[44] M. Li, L. Bao, H. Yu, and X. Zhang, "Formation of multicomponent surface nanodroplets by solvent exchange," *J. Phys. Chem. C*, vol. 122, pp. 8647–8654, 2018.

[45] Z. Lu, S. Peng, and X. Zhang, "Influence of solution composition on the formation of surface nanodroplets by solvent exchange," *Langmuir*, vol. 32, pp. 1700–1706, 2016.

[46] Z. Lu, H. Xu, H. Zeng, and X. Zhang, "Solvent effects on the formation of surface nanodroplets by solvent exchange," *Langmuir*, vol. 31, pp. 12 120–12 125, 2015.

[47] H. Tan, C. Diddens, P. Lv, J. G. Kuerten, X. Zhang, and D. Lohse, "Evaporation-triggered microdroplet nucleation and the four life phases of an evaporating ouzo drop," *Proc. Natl. Acad. Sci. U.S.A*, vol. 113, no. 31, pp. 8642–8647, 2016.

[48] B. Dyett, H. Yu, and X. Zhang, "Formation of surface nanodroplets of viscous liquids by solvent exchange," *Eur. Phys. J. E.*, vol. 40, no. 3, pp. 1–6, 2017.

[49] X. Zhang, Z. Lu, H. Tan, L. Bao, Y. He, C. Sun, and D. Lohse, "Formation of surface nanodroplets under controlled flow conditions," *Proc. Natl. Acad. Sci., USA*, vol. 112, pp. 9253–9257, 2015.

[50] Soft Matter Interfaces. (2018). "Formation of nanodroplets by solvent exchange," Youtube, [Online]. Available: https://youtu.be/gaRcfbBWp4Y (visited on 04/10/2021).

[51] D. Lohse and X. Zhang, "Physicochemical hydrodynamics of droplets out of equilibrium.," *Nat. Rev. Phys.*, vol. 2, pp. 426–443, 2020.

[52] X. H. Zhang and W. Ducker, "Formation of interfacial nanodroplets through changes in solvent quality," *Langmuir*, vol. 23, no. 25, pp. 12 478–12 480, 2007.

[53] X. Zhang, J. Ren, H. Yang, Y. He, J. Tan, and G. G. Qiao, "From transient nanodroplets to permanent nanolenses," *Soft Matter*, vol. 8, no. 16, pp. 4314–4317, 2012.

[54] L. Bao, A. R. Rezk, L. Y. Yeo, and X. Zhang, "Highly ordered arrays of femtoliter surface droplets," *Small*, vol. 11, no. 37, pp. 4850–4855, 2015.

[55] H. Yu, Z. Lu, D. Lohse, and X. Zhang, "Gravitational effect on the formation of surface nanodroplets," *Langmuir*, vol. 31, no. 46, pp. 12 628–12 634, 2015.

[56] S. Peng, D. Lohse, and X. Zhang, "Spontaneous pattern formation of surface nanodroplets from competitive growth," *ACS Nano*, vol. 9, no. 12, pp. 11 916–11 923, 2015.

[57] H. Yu, S. Peng, L. Lei, J. Zhang, T. L. Greaves, and X. Zhang, "Large scale flow-mediated formation and potential applications of surface nanodroplets," *ACS Appl. Mater. Interfaces*, vol. 8, no. 34, pp. 22 679–22 687, 2016.

[58] M. Tagavifar, K. Xu, S. H. Jang, M. T. Balhoff, and G. A. Pope, "Spontaneous and flow-driven interfacial phase change: Dynamics of microemulsion formation at the pore scale.," *Langmuir*, vol. 33, pp. 13 077–13 086, 2017.

[59] M. Hübner and M. Minceva, "Microfluidics approach for determination of the miscibility gap of multicomponent liquid-liquid systems.," *Exp. Therm. Fluid Sci.*, vol. 112, p. 109 971, 2020.

[60] M. Tomeh and X. Zhao, "Recent advances in microfluidics for the preparation of drug and gene delivery systems.," *Mol. Pharm.*, 2020.

[61] L. Wang, Y. Lin, Y. Zhou, H. Xie, J. Song, M. Li, Y. Huang, X. Huang, and S. Mann, "Autonomic behaviors in lipase-active oil droplets," *Angew. Chem., Int. Ed.*, vol. 131, pp. 1079–1083, 2019.

[62] J. W. Zwanikken, "Steering colloidal particles overmillimeter distances with soluto-inertial beacons," *Proc. Natl. Acad. Sci., USA*, vol. 113, pp. 8565–8567, 2016.

[63] F. M. Möller, F. Kriegel, M. Kieß, V. Sojo, and D. Braun, "Steep ph gradients and directed colloid transport in a microfluidic alkaline hydrothermal pore," *Angew. Chem. Int. Ed.*, vol. 56, no. 9, pp. 2340–2344, 2017.

[64] S. Das, O. E. Shklyaev, A. Altemose, H. Shum, I. Ortiz-Rivera, L. Valdez, T. E. Mallouk, A. C. Balazs, and A. Sen, "Harnessing catalytic pumps for directional delivery of microparticles in microchambers," *Nat. Commun.*, vol. 8, p. 14 384, 2017.

[65] J. F. Brady, "Particle motion driven by solute gradients with application to autonomous motion: Continuum and colloidal perspectives.," *J. Fluid Mech*, vol. 667, pp. 216–259, 2011.

[66] B. Selva, L. Daubersies, and J. B. Salmon, "Solutal convection in confined geometries: Enhancement of colloidal transport," *Phys. Rev. Lett*, vol. 108, p. 198 303, 2012.

[67] A. B. Grommet, M. Feller, and R. Klajn, "Chemical reactivity under nanoconfinement.," *Nat. Nanotechnol.*, vol. 15, pp. 256–271, 2020.

[68] A. Fallah-Araghi, K. Meguellati, J. C. Baret, A. El Harrak, T. Mangeat, M. Karplus, S. Ladame, C. M. Marques, and A. D. Griffiths, "Enhanced chemical synthesis at soft interfaces: A universal reaction-adsorption mechanism in microcompartments.," *Phys. Rev. Lett.*, vol. 112, p. 028 301, 2014.

[69] J. Cejkova, M. Novak, F. Stepanek, and M. M. Hanczyc, "Dynamics of chemotactic droplets in salt concentration gradients," *Langmuir*, vol. 30, pp. 11 937–11 944, 2014.

[70] D. Liu, A. Mahmood, D. Weng, and J. Wang, "Life-like motion of oil drops at the air-liquid interface," *Langmuir*, vol. 35, pp. 16 146–16 152, 2019.

[71] I. Lagzi, S. Soh, P. J. Wesson, K. P. Browne, and B. A. Grzybowski, "Maze solving by chemotactic droplets," *J. Am. Chem. Soc.*, vol. 132, no. 4, pp. 1198–1199, 2010.

[72] C. Jin, C. Krüger, and C. C. Maass, "Chemotaxis and autochemotaxis of self-propelling droplet swimmers.," *Proc. Natl. Acad. Sci. U.S.A.*, vol. 114, pp. 5089–5094, 2017.

[73] B. Liebchen and H. Löwen, "Synthetic chemotaxis and collective behavior in active matter," *Acc. Chem. Res.*, vol. 51, no. 12, pp. 2982–2990, 2018.

[74] S. Thutupalli, R. Seemann, and S. Herminghaus, "Swarming behavior of simple model squirmers.," *New J. Phys.*, vol. 13, p. 073 021, 2011.

[75] C. Krueger, C. Bahr, S. Herminghaus, and C. C. Maass, "Dimensionality matters in the collective behaviour of active emulsions," *Eur. Phys. J. E*, vol. 39, no. 6, pp. 1–9, 2016.

[76] Z. Izri, M. N. Van Der Linden, S. Michelin, and O. Dauchot, "Self-propulsion of pure water droplets by spontaneous marangoni-stress-driven motion," *Phys. Rev. Lett.*, vol. 113, no. 24, p. 248 302, 2014.

[77] F. Yang, S. Shin, and H. Stone, "Diffusiophoresis of a charged drop," *J. Fluid Mech.*, vol. 852, pp. 37–59, 2018.

[78] Y. Li, C. Diddens, A. Prosperetti, K. Chong, X. Zhang, and D. Lohse, "Bouncing oil droplet in a stratified liquid and its sudden death.," *Phys. Rev. Lett.*, vol. 122, p. 154 502, 2019.

[79] N. J. Cira, A. Benusiglio, and M. Prakash, "Vapour-mediated sensing and motility in two-component droplets.," *Nature*, vol. 519, pp. 446–450, 2015.

[80] M. Frenkel, V. Multanen, R. Grynyov, A. Musin, Y. Bormashenko, and E. Bormashenko, "Camphor-engine-driven micro-boat guides evolution of chemical gardens," *Sci. Rep.*, vol. 7, p. 3930, 2017.

[81] S. Shin, E. Um, B. Sabass, J. Ault, M. Rahimi, P. Warren, and H. A. Stone, "Size-dependent control of colloid transport via solute gradients in dead-end channels," *Proc. Natl. Acad. Sci., USA*, vol. 113, pp. 257–261, 2016.

[82] A. Kar, T. Y. Chiang, I. Ortiz-Rivera, A. Sen, and D. Velegol, "Enhanced transport into and out of dead-end pores," *ACS Nano*, vol. 9, pp. 746–753, 2015.

[83] T. Ban, T. Yamagami, H. Nakata, and Y. Okano, "Ph-dependent motion of self-propelled droplets due to marangoni effect at neutral ph," *Langmuir*, vol. 29, pp. 2554–2561, 2013.

[84] S. Tanaka, S. Nakata, and M. Nagayama, "A surfactant reaction model for the reciprocating motion of a self-propelled droplet," *Soft Matter*, vol. 17, no. 2, pp. 388–396, 2021.

[85] S. Herminghaus, C. C. Maass, C. Krüger, S. Thutupalli, L. Goehring, and C. Bahr, "Interfacial mechanisms in active emulsions," *Soft Matter*, vol. 10, no. 36, pp. 7008–7022, 2014.

[86] Z. Lu, A. Rezk, F. Jativa, L. Yeo, and X. Zhang, "Dissolution dynamics of a suspension droplet in a binary solution for controlled nanoparticle assembly," *Nanoscale*, vol. 9, pp. 13 441–13 448, 36 2017.

[87] J. D. Wang, N. J. Douville, S. Takayama, and M. ElSayed, "Quantitative analysis of molecular absorption into pdms microfluidic channels," *Ann. Biomed. Eng.*, vol. 40, no. 9, pp. 1862–1873, 2012.

[88] H. Yang and Å. C. Rasmuson, "Phase equilibrium and mechanisms of crystallization in liquid–liquid phase separating system," *Fluid Phase Equilib.*, vol. 385, pp. 120–128, 2015.

[89] M. Li, H. Yu, L. Bao, B. Dyett, and X. Zhang, "Controlled addition of new liquid component into surface droplet arrays by solvent exchange," *J. Colloid Interface Sci.*, vol. 543, pp. 164–173, 2019.

[90] M. Rahman, M. Rahman, and M. Nabi, "Ternary liquid equilibria of ethanol-water-oleyl alcohol and etha-nol-water-oleic acid systems," *Biological Sciences-PJSIR*, vol. 46, no. 6, pp. 409–413, 2003.

[91] X. Zhang and W. Ducker, "Interfacial oil droplets.," *Langmuir*, vol. 24, pp. 110–115, 2008.

[92] T. Lopian, S. Schöttl, S. Prevost, S. Pellet-Rostaing, D. Horinek, W. Kunz, and T. Zemb, "Morphologies observed in ultraflexible microemulsions with and without the presence of a strong acid," *ACS Cent. Sci.*, vol. 2, no. 7, pp. 467–475, 2016.

[93] K. Pratt and W. Wakeham, "The mutual diffusion coefficient of ethanol-water mixtures: Determination by a rapid, new method.," *Proc. R. Soc. Lond.*, vol. 336, pp. 393–406, 1974.

[94] K. Kinoshita, E. Parra, and D. Needham, "New sensitive micro-measurements of dynamic surface tension and diffusion coefficients: Validated and tested for the adsorption of 1-octanol at a microscopic air-water interface and its dissolution into water.," *J. Colloid Interface Sci.*, vol. 488, pp. 166–179, 2017.

[95] J. Su, P. Duncan, A. Momaya, A. Jutila, and D. Needham, "The effect of hydrogen bonding on the diffusion of water in n-alkanes and n-alcohols measured with a novel single microdroplet method.," *J. Chem. Phys.*, vol. 132, p. 044 506, 2010.

[96] O. Diat, M. L. Klossek, D. Touraud, B. Deme, I. Grillo, W. Kunz, and T. Zemb, "Octanol-rich and water-rich domains in dynamic equilibrium in the pre-ouzo region of ternary systems containing a hydrotrope," *J. Appl. Crystallogr.*, vol. 46, no. 6, pp. 1665–1669, 2013.

[97] S. Schoettl, J. Marcus, O. Diat, D. Touraud, W. Kunz, T. Zemb, and D. Horinek, "Emergence of surfactant-free micelles from ternary solutions," *Chem. Sci.*, vol. 5, no. 8, pp. 2949–2954, 2014.

[98] S. Prevost, T. Lopian, M. Pleines, O. Diat, and T. Zemb, "Small-angle scattering and morphologies of ultra-flexible microemulsions," *J. Appl. Crystallogr.*, vol. 49, no. 6, pp. 2063–2072, 2016.

[99] X. Zhang, J. B. You, G. F. Arends, J. Qian, Y. Chen, D. Lohse, and J. Shaw, "Propelling microdroplets generated and sustained by liquid-liquid phase separation in confined spaces," *Soft Matter*, 2021.

[100] Y. Li, C. Diddens, A. Prosperetti, and D. Lohse, "Marangoni instability of a drop in a stably stratified liquid," *Phys. Rev. Lett.*, vol. 126, no. 12, p. 124 502, 2021.

[101] C. Diddens, Y. Li, and D. Lohse, "Competing marangoni and rayleigh convection in evaporating binary droplets," *J. Fluid Mech.*, vol. 914, 2021.

[102] C. Liu, M. Zhao, Y. Zheng, L. Cheng, J. Zhang, and C. A. T. Tee, "Coalescence-induced droplet jumping," *Langmuir*, vol. 37, no. 3, pp. 983–1000, 2021.

[103] K. Wang, R. Li, Q. Liang, R. Jiang, Y. Zheng, Z. Lan, and X. Ma, "Critical size ratio for coalescence-induced droplet jumping on superhydrophobic surfaces," *Appl. Phys. Lett.*, vol. 111, no. 6, p. 061 603, 2017.

[104] C.-H. Chen, Q. Cai, C. Tsai, C.-L. Chen, G. Xiong, Y. Yu, and Z. Ren, "Dropwise condensation on superhydrophobic surfaces with two-tier roughness," *Appl. Phys. Lett.*, vol. 90, no. 17, p. 173 108, 2007.

[105] Y. Chen and Y. Lian, "Numerical investigation of coalescence-induced self-propelled behavior of droplets on non-wetting surfaces," *Phys. Fluids*, vol. 30, no. 11, p. 112 102, 2018.

[106] C. Lv, P. Hao, Z. Yao, Y. Song, X. Zhang, and F. He, "Condensation and jumping relay of droplets on lotus leaf," *Appl. Phys. Lett.*, vol. 103, no. 2, p. 021 601, 2013.

[107] F. Wodlei, J. Sebilleau, J. Magnaudet, and V. Pimienta, "Marangoni-driven flower-like patterning of an evaporating drop spreading on a liquid substrate," *Nat. Commun.*, vol. 9, p. 820, 2018.

[108] S. Rafaï, D. Sarker, V. Bergeron, J. Meunier, and D. Bonn, "Superspreading: Aqueous surfactant drops spreading on hydrophobic surfaces," *Langmuir*, vol. 18, no. 26, pp. 10 486–10 488, 2002.

[109] U. Weidlich and J. Gmehling, "A modified unifac model. 1. prediction of vle, he, and. gamma.. infin.," *Ind. Eng. Chem*, vol. 26, pp. 1372–1381, 1987.

[110] J. Gmehling, J. Li, and M. Schiller, "A modified unifac model. 2. present parameter matrix and results for different thermodynamic properties," *Ind. Eng. Chem*, vol. 32, pp. 178–193, 1993.

Appendix A: Supporting Information for Chapter 3

A.1 Supporting figures

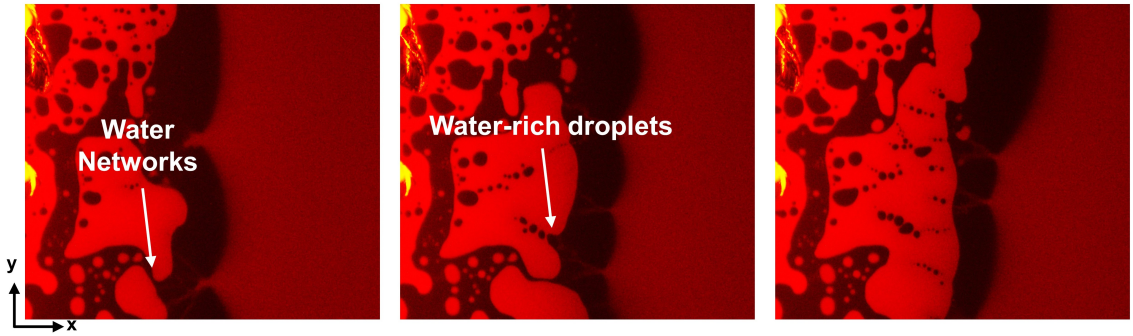

Figure A.1: Optical images showing early development of the water-rich zone 2 within Regime 3 conditions.

A.2 Supporting videos

Video S1: Bright-field imagery of boundary displacement at Regime 1 (50% 1-octanol by mass in Solution A) condition. Video shows boundary undulation and microdomain formation.

Video S2: Bright-field imagery of boundary displacement at Regime 2 (40% 1-octanol by mass in Solution A) condition. Video shows boundary undulation and stagnant droplets left behind by the boundary.

Video S3: Boundary displacement at Regime 3 (30% 1-octanol by mass in Solution A) condition. Video from 0 to 8 seconds shows the fluorescence images of the three-zone configuration at the boundary. From 8 to 20 seconds, the fluorescence mode was

changed to bright-field imaging.

Video S4: Boundary displacement at Regime 4 (10% 1-octanol by mass in Solution A) condition. Video showing the transition from a triangular protrusion in the boundary to a line-shaped protrusion. From 0 to 5, the video was in fluorescence mode, and from 5 to 25, it was in bright-field mode.

Video files are available on the ACS website: https://pubs.acs.org/doi/suppl/10.1021/acs.energyfuels.1c00139/suppl_file/ef1c00139_si_001.zip

Appendix B: Thermodynamic calculations of excess free energy from phase separation

Calculations were performed to approximate the excess energy that is released from liquid-liquid phase separation as both solution A and B mix. The 1-octanol ternary mixture was used as the representative system for our modelling with an activity coefficient model. The modified UNIFAC model or Dortmund UNIFAC model [109, 110] was used as the main thermodynamic model to determine the phase behaviour. For the simulations, we utilized both Symmetry Process Simulation software (mass balances) and a MATLAB code (energy balances) based on two works by Fredenslund and Weidlich. The Van der Waals properties of the functional groups shown in Figure B.1A, such as the group volume R_k, the surface area Q_k are in Table B.1, and the interaction parameters (a_{nm}, b_{nm}, c_{nm}) are to be found in Table B.2, Table B.3 and Table B.4.

At 5% condition, we chose the water-rich phase to be around 75 times the amount of the created 1-octanol-rich phase. This was done to have a non-equilibrium composition close to the binodal curve that may approximate the true condition as phase separation occurs in confinement. An example of two initial compositions is depicted in Figure B.1B. Symmetry is a process design software, meaning every calculation is in terms of a flowrate. To simulate our conditions, we had to fix the initial solution A feed to be a specific mass flowrate quantity. Only solution B was changed for the different initial conditions. The changes in the mass flow rates of B were all decided

by a proportionality factor based on an initial optimized value. The proportions are all tabulated with the corresponding phase compositions in Table B.5. The mass balance simulations were performed using a mixer unit in the program at $T = 25°C$ and $P = 101.3$ kPa.

The compositions from the Symmetry simulations in Table B.6 were then used in the MATLAB code that was created to only calculate the excess enthalpy as a function of the composition of each component. The UNIFAC equations used for the MATLAB code are to be found in Appendix B. We calculated the excess enthalpy of each bulk phase, water-rich and 1-octanol-rich phases. The equilibrium energy states were calculated by summation of each water and 1-octanol-rich phase with their specific fraction in the final state. The non-equilibrium energy states were calculated using the bulk-phase composition. The calculated excess enthalpy values are shown in Figure B.1C. With these values, it was possible to calculate the energy released for each initial composition, which should provide a positive value for every case.

Table B.1: Modified UNIFAC Van der Waals parameters of functional groups used in simulation for 1-octanol system.

Functional Group	**Classification**	**Group Volume**, R_k	**Surface Area**, Q_k
Methyl	Main group (n): 1 (-CH_2), Sub-group (m): 1 (-CH_3)	0.6325	1.0608
Methylene	Main group (n): 1 (-CH_2), Sub-group (m): 2 (-CH_3)	0.6325	0.7081
Hydroxide	Main group (n): 5 (-OH), Sub-group (m): 14 (Primary)	1.2302	0.8927
Water	Main group (n): 7 (-OH), Sub-group (m): 16 (Primary)	1.7334	2.4561

Table B.2: UNIFAC modified interaction parameters a_{nm} used in simulation for 1-octanol system.

	CH_3	CH_2	OH	H_2O
CH_3	0	0	2777	1391.3
CH_2	0	0	2777	1391.3
OH	1606	1606	0	-801.9
H_2O	-17.253	-17.253	1460	0

Table B.3: UNIFAC modified interaction parameters b_{nm} used in simulation for 1-octanol system.

	CH_3	CH_2	OH	H_2O
CH_3	0	0	-4.674	-3.6156
CH_2	0	0	-4.674	-3.6156
OH	-4.746	-4.746	0	3.824
H_2O	0.8389	0.8389	-8.673	0

Table B.4: UNIFAC modified interaction parameters c_{nm} used in simulation for 1-octanol system.

	CH_3	CH_2	OH	H_2O
CH_3	0	0	0.001551	0.001144
CH_2	0	0	0.001551	0.001144
OH	0.0009181	0.0009181	0	-0.007514
H_2O	0.0009021	0.0009021	0.01641	0

Table B.5: The multiplier factors were used with the initial flowrate of the 5 % 1-octanol condition as the basis, which was found to be 1.9 m^3/h from optimization with a fixed Solution A flowrate of 1 m^3/h. The optimization was based on having the set initial condition of 75 times the mass amount of water-phase to 1-octanol-rich phase.

Condition	**Multiplier**	**Solution A** m^3/h	**Solution B** m^3/h
5/48/47	1	1.00	1.90
8/47/45	0.625	1.00	1.19
10/48/42	0.5	1.00	0.95
15/48/37	0.333	1.00	0.63
20/48/32	0.25	1.00	0.48
30/48/22	0.167	1.00	0.32
40/45/15	0.125	1.00	0.24
50/40/10	0.1	1.00	0.19

Table B.6: Compositions obtained from Symmetry for simulations described in terms of mass percentage 1-octanol/ethanol/water.

Condition	**Bulk Phase**	**Water-rich Phase**	**Octanol-rich Phase**	**W/O Fraction**
5/48/47	1.6/15.2/83.2	0.6/15.1/84.2	71.4/19.1/9.5	98.7/1.3
8/47/45	3.4/20.0/76.7	0.9/19.8/79.3	64.2/24.5/11.4	96.1/3.9
10/48/42	4.8/23.0/72.3	1.2/22.6/76.2	59.7/27.6/12.7	93.9/6.1
15/48/37	8.7/27.7/63.7	1.7/27.0/71.3	53.1/32.1/14.8	86.5/13.5
20/48/32	12.9/30.9/56.3	2.1/17.2/80.3	49.0/34.8/16.3	77.1/22.9
30/48/22	21.8/34.9/43.4	2.7/32.6/64.6	44.4/37.5/18.1	54.3/45.7
40/45/15	31.1/35.0/33.9	2.5/31.7/65.7	45.8/36.7/17.5	34.0/66.0
50/40/10	40.6/32.5/26.9	1.9/28.5/69.6	50.9/33.6/15.6	20.9/79.1

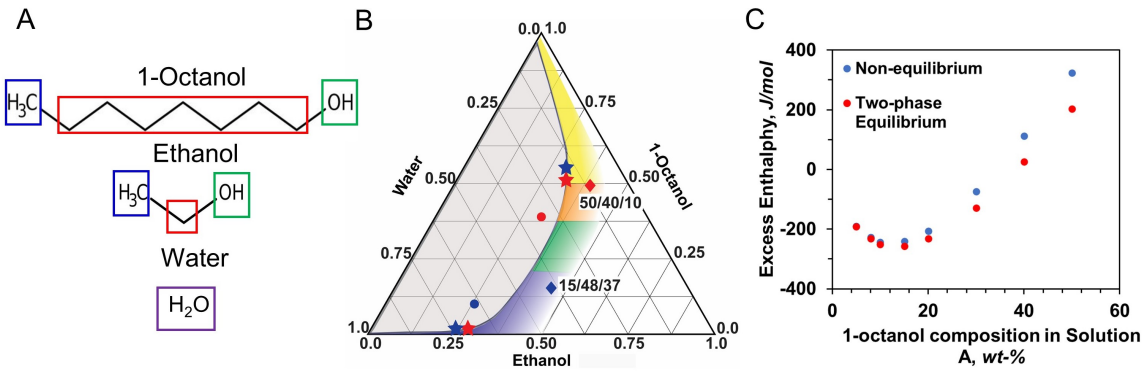

Figure B.1: (A) Chemical structure of compounds in the system with colour-coded functional groups used in modified UNIFAC calculations of enthalpy of mixing. Blue (methyl), red (methylene), green (hydroxide), and purple (water). (B) Phase diagram of a 1-octanol system showing two of the bulk compositions that were used to calculate the excess enthalpy energy of the different initial compositions, one at a low 1-octanol concentration (blue) and high 1-octanol concentration (red). Initial compositions (diamond shape), 1-octanol-rich and water-rich subphases (star), and bulk compositions (circles) are all shown in this figure. Adapted from *ACS Cent. Sci.* **2016**, 2, 7, 467–475 [92]. (C) Calculated excess enthalpy with Dortmund UNIFAC method. Blue data indicates excess enthalpy of the mixture at a non-equilibrium state. Red data indicates excess enthalpy of the mixture at equilibrium state obtained by summation of the enthalpy state of both 1-octanol-rich subphase and water-rich subphase in equilibrium.

Appendix C: Code for excess enthalpy calculations of Appendix B

For the UNIFAC calculations, we used the following equations to calculate the excess enthalpy from phase separation[1] [109, 110].

Group area fraction:

$$\theta_m = \frac{Q_m X_m}{\sum_n Q_n X_n} \tag{C.1}$$

Group mole fraction:

$$X_m = \frac{\sum_j \nu_m{}^{(j)} x_j}{\sum_j \sum_n \nu_n{}^{(j)} x_j} \tag{C.2}$$

Excess enthalpy:

$$h^E = -RT \sum_i \sum_k x_i v_k{}^{(i)} \left[T \left(\frac{\partial \ln \Gamma_k}{\partial T} \right)_{P,x} - T \left(\frac{\partial \ln \Gamma_k{}^{(i)}}{\partial T} \right)_{P,x} \right] \tag{C.3}$$

where

$$T \left(\frac{\partial \ln \Gamma_k}{\partial T} \right)_{P,x} = Q_k \sum_m \theta_m \left[\frac{(b_{mk} + \ln \Psi_{mk} + 2c_{mk}T)\Psi_{mk}}{\sum_n \theta_n \Psi_{nk}} + \ldots \right. \tag{C.4}$$
$$\left. \frac{\Psi_{km} \sum_n \theta_n \Psi_{nm}}{(\sum_n \theta_n \Psi_{nm})^2} \left[b_{km} - b_{nm} + \ln(\Psi_{km}/\Psi_{nm}) + (c_{km} - c_{nm}) 2T \right] \right]$$

The expression given by (C.4) is also valid for pure substances:

$$T \left(\frac{\partial \ln \Gamma_k{}^{(i)}}{\partial T} \right)_{P,x} \tag{C.5}$$

Temperature-dependent interaction parameter:

$$\Psi_{nm} = \exp(-(a_{nm} + b_{nm}T + c_{nm}T^2)/T) \tag{C.6}$$

[1] For a complete description of the parameters and variables, refer to the List of Symbols

Listing C.1: MATLAB code for excess enthalpy calculation using Dortmund UNIFAC Model. Based on ref [109, 110].

```
clc
clear
format short g %number formatting

%%%%%%%%%%%%%%%%%%%%%%%%%%%%%%%%%%%%%%%%%%%%%%%%%%%%%%%%%%%%%%%%%%%%%%%%%%%%%%%
%%%%%%%%%%%%% INPUT NECESSARY VALUES IN THE UPCOMING SECTIONS %%%%%%%%%%%%%
%%%%%%%%%%%%%%%%%%%%%%%%%%%%%%%%%%%%%%%%%%%%%%%%%%%%%%%%%%%%%%%%%%%%%%%%%%%%%%%
T = 298.15; % Temperature in K

% Molar composition of chemical species
%Example below: 1-Octanol Ethanol Water
xmix = [0.124422836 0.281378351 0.5941988]; %ternary mixture composition

% Van der Waals surface area interaction parameter
%(found in Dortmund UNIFAC tables)
% Functional groups in order of matrix: CH3 (C1) CH2 (C2) OH (C3) H2O (C4)
Q=[1.0608 0.7081 0.8927 2.4561];

% Nu: Number of functional groups within molecule (must be in order of Q)
% Column 1: 1-Octanol Example: 1x CH3, 7x CH2, 1x OH, 0x H2O
% Column 2: Ethanol
% Column 3: Water
Nu = [1 7 1 0;1 1 1 0;0 0 0 1];

% Interaction parameters a, b and c between functional groups n and m
% Main group number necessary to obtain values from UNIFAC table
% Example: CH3 (1), CH2 (1), OH (5), H2O (7)
%Interaction between same group is 0
%Matrix looks like:
% anm = [a11 a11 a15 a17;
%       a11 a11 a15 a17;
%       a51 a51 a55 a57;
%       a71 a71 a75 a77]

anm = [0 0 2777 1391.3;
0 0 2777 1391.3;
1606 1606 0 -801.9;
-17.253 -17.253 1460 0];

bnm = [0 0 -4.674 -3.6156;
0 0 -4.674 -3.6156;
-4.746 -4.746 0 3.824;
0.8389 0.8389 -8.673 0];

cnm = [0 0 0.001551 0.001144;
0 0 0.001551 0.001144;
0.0009181 0.0009181 0 -0.007514;
0.0009021 0.0009021 0.01641 0];


%%%%%%%%%%%%%%%%%%%%%%%%%%%%%%%%%%%%%%%%%%%%%%%%%%%%%%%%%%%%%%%%%%%%%%%%%%%%%%%
%%%%%%%%%%%%%%%%% NO NEED TO MODIFY CODE AFTER THIS POINT %%%%%%%%%%%%%%%%%
%%%%%%%%%%%%%%%%%%%%%%%%%%%%%%%%%%%%%%%%%%%%%%%%%%%%%%%%%%%%%%%%%%%%%%%%%%%%%%%
nusize = size(Nu); % Size of Nu matrix for ternary solution

xmixsize = size(xmix); % Size of x matrix for ternary solution

xpure = eye(xmixsize(2)); % pure chemical species composition matrix

% combined mixture and pure chemical species composition matrix
x=[xmix;xpure];

xsize=size(x);

% Temperature dependent interaction matrix (MOD. UNIFAC)
```

```
psi = exp(-(anm+bnm*T+cnm*T^2)/T);

% Provides total number of functional groups in a molecule
numpermolecule = sum(Nu,2);

% Group mole fraction Xm calculation for residual calculation
for l = 1:xsize(1) %from mixture to each pure substance
    for m = 1:nusize(2)
        for j = 1:xsize(2)
            NUM(j) = Nu(j,m)*x(l,j);
        end
        CALC1 = sum(NUM);
        for i = 1:xsize(2)
            DENOM(i) = x(l,i)*numpermolecule(i);
        end
        CALC2 = sum(DENOM);
        Xgroups(l,m) = CALC1/CALC2;
    end
end

% Theta calculation
for l = 1:xsize(1)
    for m = 1:nusize(2)
        theta(l,m) = Q(m).*Xgroups(l,m)/sum(Q.*Xgroups(l,:));
    end
end

for l = 1:xsize(1) %given x specie
    for k = 1:nusize(2)
        for m = 1:nusize(2)
            for n = 1:nusize(2)
                DENOM1(n) = theta(l,n)*psi(n,k);
            end

            NUM = (bnm(m,k) + log(psi(m,k)) + 2*cnm(m,k)*T)*psi(m,k);

            TERM1(l,m) = NUM/(sum(DENOM1));

            for n = 1:nusize(2)
                DENOM2(l,n) = theta(l,n).*psi(n,m);
            end

            for n = 1:nusize(2)
                TERM2(l,n) = theta(l,n)*psi(n,m)*(bnm(k,m)-bnm(n,m)+...
                    log(psi(k,m)/psi(n,m))+(cnm(k,m)-cnm(n,m))*2*T);
            end

            TERM3(l,m) = theta(l,m)*(TERM1(l,m)+ psi(k,m)*...
                sum(TERM2(l,:))/(sum(DENOM2(l,:)))^2);

        end
        dgamma(l,k) = Q(k).*sum(TERM3(l,:));
    end
end

%dgamma for components
for i = 1:xsize(1)-1
    dgamma_comp(i,:) = dgamma(1,:) - dgamma(i+1,:);
end


for i = 1:xsize(2)
    for k = 1:nusize(2)
        SUM(k) = x(1,i)*Nu(i,k)*(dgamma_comp(i,k));
    end
    SUM1(i) = sum(SUM);
end
```

```
SUM2 = sum(SUM1);
h = -8.314*T*SUM2
```